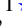



Ice origins of OCS and chemistry of CS₂-bearing ice mantles

Rafael Martín-Doménech,¹   Karin I. Öberg,² Guillermo M. Muñoz Caro,¹ Héctor Carrascosa,¹ Asunción Fuente¹, Mahesh Rajappan²

¹Centro de Astrobiología (CSIC-INTA) Carretera de Ajalvir, km. 4, Torrejón de Ardoz, E-28850, Madrid, Spain

²Center for Astrophysics | Harvard & Smithsonian, 60 Garden St., Cambridge, MA 02138, USA

Accepted XXX. Received YYY; in original form ZZZ

ABSTRACT

Understanding the formation of carbonyl sulfide (OCS) in interstellar ices is key to constrain the sulfur chemistry in the interstellar medium (ISM), since it is the only ice S-bearing molecule securely detected thus far. Two general pathways for OCS formation have been proposed: sulfurization of CO (CO+S) and oxidation of CS (CS+O), but their relative contribution in interstellar ices remains unconstrained. We have evaluated the contribution of both pathways to OCS formation upon energetic processing in isotopically-labeled CO₂:CS₂ and CO:CS₂ ice samples at 7–50 K. Our results indicated that formation of OCS through the CS+O pathway was more favorable than through the CO+S pathway, as previously suggested by theoretical calculations. In addition, its relative contribution increased at higher temperatures. Therefore, this pathway could play a role in the ice formation of OCS, especially in warm regions where CO is expected to be preferentially in the gas phase. At the same time, we have explored the chemistry of CS₂-bearing, CO₂-, CO-, and also H₂O-rich ices, that could be relevant to the sulfur interstellar chemistry. We observed formation of a variety of S-bearing products in addition to OCS, including SO₂, C₃S₂, and S₂. However, a significant fraction of sulfur was not detected at the end of the experiments, and could be locked in long, undetectable sulfur allotropes, one of the potential carriers of the missing sulfur in the dense ISM.

Key words: astrochemistry; solid state: volatile; ISM: clouds; ISM: molecules

1 INTRODUCTION

Sulfur (S) is the tenth most abundant element in the universe (S/H $\sim 1.5 \times 10^{-5}$, Asplund et al. 2009), and it is present in a variety of biomolecules on Earth (amino acids, nucleic acids, vitamins). Despite its relevance, the fate of sulfur in the interstellar medium (ISM) once it is incorporated into the interior of dense clouds is uncertain (see, e.g., Laas & Caselli 2019, and references therein). Most of the sulfur in the dense ISM is expected to be locked in the solid phase, either on ice mantles or in (semi-)refractory form (Millar & Herbst 1990; Ruffle et al. 1999; Vidal et al. 2017; Drozdovskaya et al. 2018; Kama et al. 2019; Fuente et al. 2019; Rivière-Marichalar et al. 2020; Fuente et al. 2023). However, detections of solid sulfur in these regions have been sparse. In interstellar ices, only carbonyl sulfide (OCS) has been securely detected (see, e.g., Boogert et al. 2022; McClure et al. 2023), while the presence of sulfur dioxide (SO₂) has also been suggested (most recently in Rocha et al. 2024). Unfortunately, their reported abundances only account for <5% of the cosmic sulfur abundance.

Even though they do not represent the main sulfur carrier in the dense ISM, understanding how this reservoir of sulfur in interstellar ices is built would be of vital importance to constrain the sulfur chemistry in the ISM. In the case of OCS, direct accretion from the gas

phase is probably not significant, based on its low gas-phase abundance with respect to CO compared to the OCS/CO ratio measured in ices (see, e.g., Boogert et al. 2022). Therefore, *in situ* formation on the grain surface or the ice bulk is usually invoked. Two general pathways for OCS formation have been presented in the literature: sulfurization of CO (CO+S) and oxidation of CS (CS+O). Adriaens et al. (2010) theoretically studied the atom-addition reactions CO + S and CS + O, as well as the neutral-radical reactions CO + HS and CS + OH, both in the gas phase and on coronene (as an analog to carbonaceous dust grains). The results showed that for both, the atom-addition and the neutral-radical reactions, oxidation of CS was more energetically favorable than sulfurization of CO. In any case, the authors indicated that the dominant OCS formation route in the ISM would depend not only on the efficiency and rate of the reactions, but also on the availability of the reactants.

Formation of OCS in interstellar ices has been studied in the laboratory under astrophysically relevant conditions. The sulfurization of CO was first explored in Ferrante et al. (2008) and Garozzo et al. (2010). These authors performed 800 and 200 keV (respectively) proton irradiation experiments at 10–20 K of ice samples containing CO and either SO₂ or hydrogen sulfide (H₂S) as the S-source. H₂S has not yet been detected in interstellar ices, but it is the most abundant S-bearing molecule in comets (see, e.g., Calmonte et al. 2016). OCS formation was observed in both cases. Ferrante et al. (2008) also performed experiments with CO₂ as the CO source and observed a decrease in the OCS formation efficiency. This suggested that dissociation of the CO₂ molecules (in addition to dissociation

* E-mail: rmartin@cab.inta-csic.es

† The reported experiments were performed during an internship at the Center for Astrophysics | Harvard & Smithsonian.

of the S-carrier) was required prior to the formation of OCS through the atom-addition reaction



Irradiation of CO:H₂S and CO₂:H₂S ice samples at 14 K was carried out in [Chen et al. \(2015\)](#) using vacuum and extreme ultraviolet (VUV and EUV) photons. The results were similar to those reported in [Ferrante et al. \(2008\)](#). Experiments with different initial ice compositions revealed that formation of OCS competed with formation of H₂S₂ (the latter being favored in samples with higher H₂S abundances). Therefore, [Chen et al. \(2015\)](#) suggested that, when H₂S is the S-source, formation of OCS may proceed through both, the atom-addition (Eq. 1) and the neutral-radical reaction:



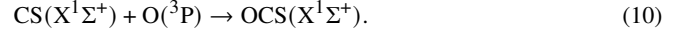
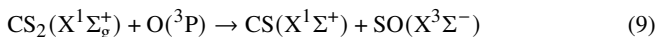
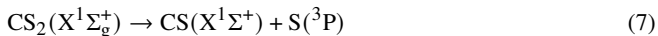
The CO + HS reaction has recently been revisited in [el Akel et al. \(2022\)](#) during co-deposition of CO, H₂S, and H atoms on a substrate at 10 K and 22 K. According to these works, the neutral-radical reaction takes place in two steps:



On the other hand, the oxidation of CS was explored in [Ward et al. \(2012\)](#) and [Maity & Kaiser \(2013\)](#) using carbon disulfide (CS₂) as the CS source in both cases. Even though CS₂ is readily formed in the laboratory upon irradiation of CO:H₂S ice mixtures (see [Ferrante et al. 2008](#); [Garozzo et al. 2010](#); [Chen et al. 2015](#)), this molecule has not yet been detected in interstellar ices, perhaps due to its subsequent conversion to other S-bearing species ([Ward et al. 2012](#); [Maity & Kaiser 2013](#)). In the Solar System, CS₂ has been detected in comets ([Calmonte et al. 2016](#)) and in planetary bodies such as the Jovian system ([Noll et al. 1995](#)). Therefore, studying the CS₂ ice chemistry could also be relevant to constrain the sulfur interstellar chemistry. [Ward et al. \(2012\)](#) studied the thermal reaction between simultaneously deposited CS₂ molecules and O atoms on a surface at 15–70 K. The formation of OCS below 25 K mainly took place through a two-step mechanism:



[Maity & Kaiser \(2013\)](#) studied the formation of OCS upon 5 keV electron irradiation of CS₂:O₂ ice mixtures at 12 K. The authors proposed a comprehensive reaction scheme that included the formation of additional S-bearing (SO₂, SO₃, C₃S₂) and non-S-bearing (CO, CO₂, O₃) molecules detected by IR spectroscopy. In particular, formation of OCS took place through the atom-addition reaction of ground (singlet) state CS with suprathreshold O atoms in the ground (triplet) state:



A similar set of reactions would be expected if a different O-bearing molecule such as H₂O or CO₂ acted as a source of O atoms ([Maity & Kaiser 2013](#)). We note that reaction 10 (and also reactions 1 and 6 when reactants are in the ground electronic state) are, in principle, spin-forbidden. [Adriaens et al. \(2010\)](#) indicated that such reactions would initially form OCS in the excited triplet state, which would be stabilized on the coronene surface and relaxed to the ground singlet state. A similar behavior would be expected in the ice. Likewise, [Okabe \(1978\)](#) suggested that reaction 7 may take place in violation of the spin conservation rules because of the presence of heavy S atoms.

Previous laboratory experiments addressing the ice formation of OCS can thus be divided in two groups: 1) those studying the sulfurization of CO in ice samples containing CO or CO₂ and a S-source (either SO₂ or H₂S), and 2) those studying the oxidation of CS in ice samples containing CS₂ and a O-source (either O atoms or irradiated O₂ molecules). [Sivaraman \(2016\)](#) reported the formation of OCS molecules in 2 keV electron irradiated CO₂:CS₂ ice samples at 85 K, but could not pinpoint whether they formed through the CO+S and/or CS+O formation pathways. In this work, we have simultaneously studied both OCS formation pathways upon 2 keV electron irradiation of ice samples containing isotopically-labeled CO or CO₂ (as a source of CO and O atoms) and CS₂ (as a source of CS and S atoms) at 7–50 K. These experiments have allowed us to i) compare the relative contribution of the CO+S and CS+O pathways in samples where both are accessible, and ii) constrain the effect of ice temperature on said pathways. Additional irradiation experiments of H₂O:CS₂ and CO:H₂S ice samples were also performed to explore both pathways in different ice environments. With these experiments we have also been able to evaluate the sulfur chemistry of ices containing CS₂ in realistic environments (H₂O, CO, and CO₂ ice matrices), which could be relevant to the sulfur interstellar chemistry. The experimental setup used for the laboratory experiments is described in Sect. 2, and the results are presented in Sect. 3. Sections 4.1 and 4.2 discuss the relative contribution of the two OCS formation pathways and their dependence with the ice temperature, while the chemistry of CS₂-bearing ices is discussed in Sect. 4.3. Finally, Sect. 4.4 summarizes the astrophysical implications of this work, and Sect. 5 lists the main conclusions.

2 METHODS

Table 1 lists the irradiation experiments carried out for this paper. The resulting ice chemistry products were detected by a combination of IR spectroscopy of the ice samples (Sect. 2.4) and quadrupole mass spectrometry of the desorbing molecules during temperature programmed desorption (TPD) of the irradiated ices (Sect. 2.5). In order to distinguish between the OCS molecules formed through the CO+S and the CS+O pathways in Experiments 1–9, we isotopically labeled the C in the initial CO and CO₂ molecules. Therefore, the OCS molecules formed through the CO+S pathway contained ¹³C, while those formed through the CS+O pathway did not. In addition, we isotopically labeled the O in the CO, CO₂, and H₂O molecules in Experiments 1–11 in order to shift the position of the IR bands and avoid overlapping with other features. As a result, the oxidation of CS led to the formation of ¹⁸OCS (with an IR feature at ~2010 cm⁻¹ and a molecular mass of 62 amu), while the sulfurization of CO led

Exp.	Ice comp.	Comp. ratio	Ice thickness (ML)	Irrad. T (K)	Irrad. Fluence ($\times 10^{18}$ eV cm $^{-2}$)
1	$^{13}\text{C}^{18}\text{O}_2\text{:CS}_2$	88:12	205	7	8.5
2	$^{13}\text{C}^{18}\text{O}_2\text{:CS}_2$	85:15	205	8	8.8
3	$^{13}\text{C}^{18}\text{O}_2\text{:CS}_2$	84:16	195	25	8.6
4	$^{13}\text{C}^{18}\text{O}_2\text{:CS}_2$	84:16	205	50	8.9
5	$^{13}\text{C}^{18}\text{O}_2\text{:CS}_2$	93:7	530	10	4.5*
6	$^{13}\text{C}^{18}\text{O}_2\text{:CS}_2$	93:7	490	11	4.3*
7	$^{13}\text{C}^{18}\text{O}\text{:CS}_2$	88:12	205	7	8.6
8	$^{13}\text{C}^{18}\text{O}\text{:CS}_2$	89:11	210	15	7.4
9	$^{13}\text{C}^{18}\text{O}\text{:CS}_2$	89:11	220	25	8.0
10	$\text{H}_2^{18}\text{O}\text{:CS}_2$	74:26	340	8	8.4
11	$\text{H}_2^{18}\text{O}\text{:CS}_2$	74:26	340	50	8.1
12	$\text{CO}\text{:H}_2\text{S}$	82:18	285	6	7.7
13	$\text{CO}\text{:H}_2\text{S}$	80:20	270	25	8.2

Table 1. Summary of the performed irradiation experiments. The ice composition ratios and thicknesses were measured at the deposition temperature (6–8 K). A 30% and 40% uncertainty (respectively) should be considered for these values (see the text). Note that 1 ML = 10^{15} molecules cm $^{-2}$. *Photon irradiation instead of electron irradiation.

to the formation of $^{18}\text{O}^{13}\text{CS}$ (with an IR feature at ~ 1955 cm $^{-1}$ and a molecular mass of 63 amu).

Experiments 1–4 and 7–13 were carried out using the SPACE TIGER experimental setup, consisting of a ultra-high-vacuum (UHV) chamber with a base pressure of $\sim 2 \times 10^{-10}$ Torr that is relevant to dense cloud interior conditions. The ice samples in Experiments 5 and 6 were irradiated with VUV photons instead of 2 keV electrons to explore the influence of the energy source in the formation of OCS molecules. These experiments were performed in the SPACE CAT setup. These setups are described in detail in Maksyutenko et al. (2022) and Lauck et al. (2015), respectively. In this Section we present those features specific to the reported experiments.

2.1 Ice sample preparation

The ice samples in Experiments 1–4 and 7–13 were deposited on a copper substrate at 6–8 K located at the center of the UHV chamber, and warmed up to the corresponding irradiation temperature when needed (fifth column of Table 1). The ices in Experiments 5 and 6 were deposited on a CsI substrate at 10–11 K and irradiated at the same temperature. In both cases, the ice samples were grown by exposing the substrate to a gas mixture with the desired composition, introduced in the chamber from an independently pumped gas line assembly. The gas mixtures were composed by a combination of $^{13}\text{C}^{18}\text{O}_2$ (gas, 95%, Sigma-Aldrich), $^{13}\text{C}^{18}\text{O}$ (gas, 99%, Sigma-Aldrich), CO (gas, 99.95%, Sigma-Aldrich), CS_2 (anhydrous, $\geq 99\%$, Sigma-Aldrich), H_2^{18}O (liquid, 99%, Sigma-Aldrich), and H_2S (gas, $\geq 99.5\%$, Sigma-Aldrich). CS_2 and H_2^{18}O were used after applying three freeze-thaw-pump cycles. The composition and thickness of the ice samples were determined by IR spectroscopy (Sect. 2.4), and are indicated in the third and fourth columns of Table 1, respectively.

2.2 2 keV electron irradiation of the ice samples

The ice samples in Experiments 1–4 and 7–15 were electron irradiated using an ELG-2/EGPS-1022 electron source system provided by Kimball Physics. The energy of the irradiated electrons was 2 keV. In the dense ISM, cosmic rays (consisting predominantly of protons) interacting with interstellar ices lose most of their kinetic energy via transfer to the electronic system of the target molecules.

This produces the so-called δ -electrons within the ice mantles, with energies of up to a few keV (Jones et al. 2011). The corresponding electronic linear energy transfer is on the order of a few keV μm^{-1} (Hovington et al. 1997), similar to that corresponding to the irradiation of ice samples in the laboratory using keV electrons (Bennett et al. 2004). In the reported experiments the electron beam current varied between 90 and 110 nA, with an average irradiation time of ~ 110 minutes, leading to a total incident energy fluence of 7.3–8.9 $\times 10^{18}$ eV cm $^{-2}$ (sixth column of Table 1). This would correspond to the energy deposited by the cosmic rays into the interstellar ice mantles in the interior of dense clouds during $\sim 5 \times 10^6$ years (see Jones et al. 2011, and references therein).

The penetration depth of the 2 keV electrons (defined as the ice thickness where 75% of the electron energy was lost) depended on the composition of the ice samples, and was calculated with the CASINO v2.42 code (Drouin et al. 2007). This value was ~ 180 ML (1 ML = 10^{15} molecules cm $^{-2}$) for the $^{13}\text{C}^{18}\text{O}_2\text{:CS}_2$ ice samples in Experiments 1–4, ~ 170 ML for the $^{13}\text{C}^{18}\text{O}\text{:CS}_2$ ice samples in Experiments 7–9, ~ 260 ML for the $\text{H}_2^{18}\text{O}\text{:CS}_2$ ice samples in Experiments 10–11, and ~ 195 ML for the $\text{CO}\text{:H}_2\text{S}$ ice samples in Experiments 12–13.

2.3 VUV photon irradiation of the ice samples

The ice samples in Experiments 5 and 6 were irradiated with VUV photons using a Hamamatsu H2D2 L11798 deuterium lamp. The lamp emission spectrum is presented in Bergner et al. (2017) and Martín-Doménech et al. (2020), and features a strong emission band at ~ 160 nm and a weaker emission around Ly α wavelengths. This resembles the secondary UV field produced in the interior of dense clouds from the interaction of cosmic rays with gas-phase H_2 molecules (Cecchi-Pestellini & Aiello 1992; Shen et al. 2004). The mean energy of the irradiated VUV photons was 7.8 eV. The VUV flux at the sample position in Experiments 5 and 6 was measured with a NIST calibrated AXUV-100G photodiode placed in front of the substrate (5.3×10^{13} and 5.1×10^{13} photons cm $^{-2}$ s $^{-1}$, respectively). The irradiation time was 180 minutes in both experiments, leading to a total fluence of 5.7×10^{17} and 5.5×10^{17} photons cm $^{-2}$, respectively. This corresponded to an incident energy fluence of 4.5×10^{18} and 4.3×10^{18} eV cm $^{-2}$ (sixth column of Table 1). For comparison, ice mantles in the interior of dense clouds are ex-

posed to a fluence of $\sim 6 \times 10^{17}$ photons cm^{-2} during 2×10^6 years, assuming an interstellar secondary UV flux of $\sim 10^4$ photons $\text{cm}^{-2} \text{s}^{-1}$ (Cecchi-Pestellini & Aiello 1992; Shen et al. 2004).

The average VUV-absorption cross section of CO_2 ice in the 120–160 nm range is $6.7 \times 10^{-19} \text{ cm}^{-2}$ (Cruz-Díaz et al. 2014), meaning that 4450 ML of CO_2 ice are needed to absorb 95% of the incident photons in that range. Unfortunately, the VUV-absorption cross section of CS_2 ice has not yet been reported. Therefore, it was not possible to estimate the absorbed energy in Experiments 5 and 6.

2.4 IR ice spectroscopy

The ice samples in Experiments 1–4 and 7–13 were monitored through reflection-absorption IR spectroscopy (RAIRS), while those in Experiments 5 and 6 were monitored through IR spectroscopy in transmittance. In both cases we used a Bruker 70v Fourier transform IR (FTIR) spectrometer with a liquid-nitrogen-cooled MCT detector. The spectra were averaged over 256 interferograms and collected with a resolution of 1 cm^{-1} in the 5000–600 cm^{-1} range.

The integrated absorbances of the detected IR features were used to estimate the ice column densities (N) in molecules cm^{-2} of the corresponding species using the equation:

$$N = \frac{1}{A} \int_{\text{band}} \tau_\nu d\nu, \quad (11)$$

where τ_ν is the optical depth of the absorption band (2.3 times the absorbance), and A is the band strength of the IR feature in cm molecule^{-1} . The IR features were numerically integrated using the `integrate.simps` function in the SciPy library. When neighboring bands overlapped, the corresponding region of the IR spectrum was fitted with multiple Gaussians using the `curve_fit` function. The integrated absorbances were then calculated as the area of the Gaussians. Table 2 lists the reported band strengths in transmittance of selected IR features in pure ices of the main isotopologs. In this work we assumed the same band strengths for the different isotopologs of the same species as a first approximation, which could introduce an uncertainty of up to 20% (Gerakines et al. 1995). In addition, the band strengths in reflection-absorption IR spectra differ from those in transmittance spectroscopy, and are setup specific. In the case of SPACE TIGER, Martín-Doménech et al. (2024) reported a ratio of ~ 2.3 for the 4253 cm^{-1} CO IR band strength in the reflection-absorption and transmittance modes, with a 35% uncertainty. This ratio has been adopted for all IR features in the present work. As a result, we estimated an absolute uncertainty of 40% in the ice column densities calculated from the IR integrated absorbances in Experiments 1–4 and 7–13. We note that only a 30% uncertainty was considered when calculating column density ratios (due to the 20% uncertainty of the individual column densities), because the ~ 2.3 ratio (carrying an additional 35% uncertainty, as explained above) was not used in that case. The initial ice thicknesses and composition ratios are listed in the third and fourth columns of Table 1.

2.5 Temperature Programmed Desorption (TPD) of the irradiated ice samples

The irradiated ice samples were warmed from the irradiation temperature (fifth column in Table 1) up to 250 K at a controlled heating rate of 2 K min^{-1} . The molecules desorbing from the ice mantles to the gas phase were detected with a Pfeiffer QMG 220M1 QMS (mass-to-charge range of 1–100 amu and 0.5 amu resolution). To this purpose, we monitored the signal corresponding to mass-to-charge

ratios (m/z) equal to the molecular mass (and/or to relevant molecular fragments) of the initial ice components and the expected ice chemistry products. The evolution of the QMS signal of desorbing species as a function of temperature is known as a TPD curve.

For those species with no detectable IR features, calibration of the QMS allowed a rough estimation of the desorbing column density ($N(X)$) from the integrated QMS signal of the corresponding TPD curve ($A(m/z)$) using Eq. 12 (Martín-Doménech et al. 2015):

$$N(X) = \frac{A(m/z)}{k_{CO}} \cdot \frac{\sigma^+(CO)}{\sigma^+(X)} \cdot \frac{F_F(28)}{F_F(m)} \cdot \frac{S(28)}{S(m/z)}, \quad (12)$$

where k_{CO} was the proportionality constant for CO molecules, $\sigma^+(X)$ was the electron-impact ionization cross-section for species X , $F_F(m)$ was the fraction of molecules X leading to a fragment of mass m in the QMS, and $S(m/z)$ was the sensitivity of the QMS to the mass fragment m/z . The k_{CO} and $S(m/z)$ parameters were derived from dedicated calibration experiments described in detail in Martín-Doménech et al. (2024). New calibration experiments were performed to update the k_{CO} value ($1.15 \times 10^{-11} \text{ A K ML}^{-1}$), and the equations to calculate $S(m/z)$:

$$k_{QMS}^* \cdot S(m/z) = 2.31 \times 10^{15} \cdot e^{-\frac{m/z}{12.38}} \quad (m/z < 40) \quad (13)$$

$$k_{QMS}^* \cdot S(m/z) = 2.37 \times 10^{14} \cdot e^{-\frac{m/z}{41.72}} \quad (m/z > 40) \quad (14)$$

(where k_{QMS}^* was a different proportionality constant that canceled out when calculating the $S(28)/S(m/z)$ ratio). A 50% uncertainty was estimated in Martín-Doménech et al. (2024) for the column densities calculated with Eq. 12.

3 RESULTS

The 2 keV electron irradiation of $^{13}\text{C}^{18}\text{O}_2:\text{CS}_2$ and $^{13}\text{C}^{18}\text{O}:\text{CS}_2$ ice samples at 7 K (Experiments 1, 2, and 7) are presented in Sections 3.1 and 3.3, respectively. These two sections first introduce an overview of the ice chemistry (with special attention to the S-bearing molecules), and then focus on the relative contribution of the CO+S and CS+O pathways to the formation of OCS. Section 3.2 presents the VUV photon irradiation of $^{13}\text{C}^{18}\text{O}_2:\text{CS}_2$ samples (Experiments 5 and 6), aimed at evaluating the effect of the energy source on the formation of OCS. Sections 3.4 and 3.5 assess the effect of the ice temperature on the relative contributions of the two OCS formation pathways in $^{13}\text{C}^{18}\text{O}_2:\text{CS}_2$ and $^{13}\text{C}^{18}\text{O}:\text{CS}_2$ samples, respectively (Experiments 3, 4, 8, 9). Finally, Sections 3.6 and 3.7 explore whether the same trends observed in previous sections apply to different ice compositions depicting other plausible astrophysical environments (Experiments 10–13).

3.1 2 keV electron irradiation of a $^{13}\text{C}^{18}\text{O}_2:\text{CS}_2$ ice sample at 7 K

Fig. 1 shows the IR difference spectrum in the 2400–600 cm^{-1} range obtained upon 2 keV electron irradiation at 7 K of the $^{13}\text{C}^{18}\text{O}_2:\text{CS}_2$ ice sample in Exp. 1. Results were comparable in Exp. 2, with a similar initial ice composition and irradiated energy fluence, (see top panel of Fig. A1 in Appendix A) Energetic processing of the ice led to dissociation of $^{13}\text{C}^{18}\text{O}_2$ and CS_2 molecules, resulting in negative features in Fig. 1, while formation of new products led to positive features. According to their corresponding IR absorbances, $\sim 27\%$

Molecule	Wavenumber (cm ⁻¹)	Band strength (cm molecule ⁻¹)	Reference
H ₂ O	760	3.1 × 10 ⁻¹⁷	Gerakines et al. (1995)
CO ₂	2343	7.6 × 10 ⁻¹⁷	Gerakines et al. (1995)
CO ₂	660	1.1 × 10 ⁻¹⁷	Gerakines et al. (1995)
CO	2139	1.1 × 10 ⁻¹⁷	Gerakines et al. (1995)
C ₃ O ₂	2242	1.3 × 10 ⁻¹⁶	Gerakines & Moore (2001)
CS ₂	1501	1.1 × 10 ⁻¹⁶	Taillard et al. (submitted)
H ₂ S	2547	1.7 × 10 ⁻¹⁷	Yarnall & Hudson (2022)
OCS	2031	1.2 × 10 ⁻¹⁶	Yarnall & Hudson (2022)
SO ₂	1323	4.2 × 10 ⁻¹⁷	Yarnall & Hudson (2022)
SO ₃	1385	3.0 × 10 ⁻¹⁷	Majkowski et al. (1978)

Table 2. Band strengths of selected features in pure ice IR spectra collected in transmittance. The same band strengths were assumed for the different isotopologs of every species as a first approximation, which could introduce an uncertainty of up to 20% (Gerakines et al. 1995). We used the 660 cm⁻¹ IR feature instead of the main feature at 2343 cm⁻¹ to estimate the ¹³C¹⁸O₂ ice column density in Experiments 1–6, because it appeared in a cleaner region of the spectrum.

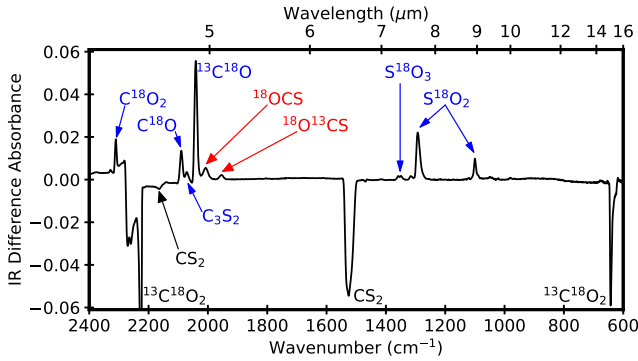


Figure 1. IR difference spectrum obtained upon 2 keV electron irradiation of a ¹³C¹⁸O₂:CS₂ ice sample at 7 K in Exp. 1. IR band assignments are indicated for the initial ice components (black), and ice chemistry products (blue), including the OCS isotopologs (red).

of the initial ¹³C¹⁸O₂ and ~60% of the initial CS₂ molecules were depleted after irradiation. The main irradiation product was ¹³C¹⁸O (detected at ~2040 cm⁻¹), most likely formed through dissociation of the ¹³C¹⁸O₂ molecules. C¹⁸O molecules were also detected at ~2090 cm⁻¹, and could be formed through dissociation of produced ¹⁸OCS molecules (Maity & Kaiser 2013) or through C + ¹⁸O atom-addition reactions. Further oxidation of the C¹⁸O molecules led to the formation of C¹⁸O₂, detected at ~2310 cm⁻¹. We note that formation of ¹³C¹⁸O₃ and ¹⁸O₃, usually detected upon energetic processing of CO₂-bearing ices (see, e.g., Ferrante et al. 2008; Chen et al. 2015), was not significant in Experiments 1 and 2. In particular, even though a very weak IR feature was tentatively observed at 983 cm⁻¹, its assignment to ¹⁸O₃ (Maity & Kaiser 2013) could not be confirmed because thermal desorption of this species was not detected during the subsequent TPD. Therefore, this feature was not marked in Figures 1 and A1. The ¹³C¹⁸O₃ IR feature, on the other hand, could be overlapped with the ¹⁸O¹³CS IR band (see Sect. 3.2). However, the ¹⁸OCS/¹⁸O¹³CS ratio calculated from the IR absorbances was similar to that obtained from the TPD curves (see below). Since the *m/z* 63 TPD curve corresponding to ¹⁸O¹³CS could not present any contribution from ¹³C¹⁸O₃ (with a molecular mass of 67 amu), we assumed that the contribution of ¹³C¹⁸O₃ to the ¹⁸O¹³CS IR feature was negligible. This could indicate that ¹⁸O atoms resulting from the dissociation of ¹³C¹⁸O₂ molecules preferentially reacted with CS₂ and its dissociation products.

On the other hand, the main detected S-bearing product was S¹⁸O₂,

with two IR features detected at 1290 and 1100 cm⁻¹ (Maity & Kaiser 2013). Thermal desorption of this molecule at T ~ 110 K was detected during the TPD of the irradiated samples, and is shown in Appendix A (bottom left panel of Fig. A2). The estimated S¹⁸O₂ ice column density after irradiation was ~8 ML. This accounted for ~16% of the initial sulfur in the ice samples, or ~26% of the sulfur consumed during irradiation. Oxidation of S¹⁸O₂ molecules led to the formation of ~1 ML of sulfur trioxide (S¹⁸O₃), detected at 1350 and 1357 cm⁻¹ (Maity & Kaiser 2013). S¹⁸O₃ accounted for ~2% of the initial sulfur, or ~4% of the consumed sulfur.

Formation of OCS molecules took place through both, the CS+O and the CO+S pathways, leading to the detection of two IR features at 2009 and 1955 cm⁻¹ (corresponding to ¹⁸OCS and ¹⁸O¹³CS, respectively). The ¹⁸OCS IR feature was detected at 2002 cm⁻¹ in Maity & Kaiser (2013), while the position of the ¹⁸O¹³CS feature had not been previously reported in the literature. The assignment of both features was confirmed during the TPD of the irradiated ice sample. The bottom left panel of Fig. 2 shows the *m/z* 62 and *m/z* 63 TPD curves corresponding to ¹⁸OCS and ¹⁸O¹³CS in Exp. 1. A desorption peak was detected at T ~ 90 K, followed by a second peak at T ~ 105 K. The ¹⁸OCS and ¹⁸O¹³CS thermal desorption resulted in a decrease of the 2009 and 1955 cm⁻¹ IR band absorbances in the same temperature range, as observed in Fig. 3. The total OCS ice column density (calculated from the sum of ¹⁸OCS and ¹⁸O¹³CS integrated IR absorbances) was ~1.5 ML, representing ~3% of the initial sulfur in the ice, or ~5% of the sulfur consumed during irradiation.

In addition to S¹⁸O₂, S¹⁸O₃, and both OCS isotopologs (accounting for ~35% of the sulfur consumed during irradiation), two additional S-bearing species were detected after irradiation of a ¹³C¹⁸O₂:CS₂ ice sample: C₃S₂ and S₂. The IR feature detected at 2070 cm⁻¹ (Figures 1 and 2) was assigned to C₃S₂ based on Maity & Kaiser (2013). Unfortunately, no band strength was found in the literature for this feature. As a first approximation, we estimated the C₃S₂ IR band strength from the C₃O₂ IR band strength in Table 2, assuming the same ratio as for the CS₂ and CO₂ main IR features. This led to a band strength of 1.8 × 10⁻¹⁶ cm molecule⁻¹, and a C₃S₂ ice column density of ~0.4 ML. On the other hand, S₂ was not detected in the IR spectrum due to its lack of dipole moment, but thermal desorption of this species was observed during the TPD (Fig. 4, left panel). S₂ molecules mainly desorbed in the 110–115 K temperature range, in agreement with the 113 K desorption temperature reported in Cazaux et al. (2022). A rough estimation of the S₂ ice column density was derived from the integrated TPD curve using Eq. 12. Using the electron-impact ionization cross-section listed in the NIST database (7.927 Å²), and assuming a fragmentation factor of 0.5 for

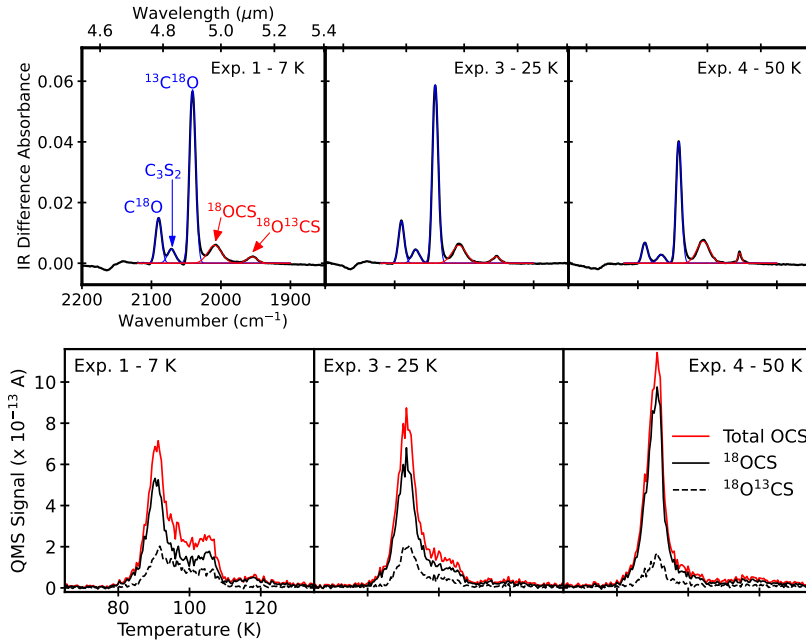


Figure 2. *Top:* Gaussian fitting of the features corresponding to C^{18}O , C_3S_2 , $^{13}\text{C}^{18}\text{O}$ (blue), ^{18}OCS and $^{18}\text{O}^{13}\text{CS}$ (red) in the IR difference spectra of the $^{13}\text{C}^{18}\text{O}_2:\text{CS}_2$ ice samples irradiated at 7 K (left panel), 25 K (middle panel), and 50 K (right panel). *Bottom:* TPD curves corresponding to ^{18}OCS (solid black) and $^{18}\text{O}^{13}\text{CS}$ (dashed black), along with the sum of both signals (solid red), measured during thermal desorption of the irradiated ice samples in the same experiments.

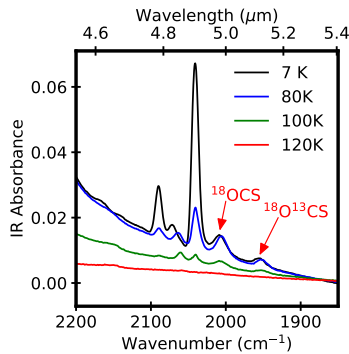


Figure 3. Evolution of the IR spectrum in the $2200\text{--}1850\text{ cm}^{-1}$ range during the TPD of the irradiated $^{13}\text{C}^{18}\text{O}_2:\text{CS}_2$ ice sample in Exp. 1.

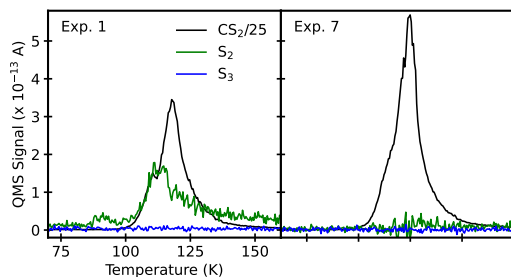


Figure 4. TPD curves corresponding to the remaining CS_2 (black), S_2 (green), and S_3 (blue) measured during thermal desorption of the irradiated $^{13}\text{C}^{18}\text{O}_2:\text{CS}_2$ ice sample in Exp. 1 (left panel), and $^{13}\text{C}^{18}\text{O}:\text{CS}_2$ ice sample in Exp. 7 (right panel).

S_2 as a first approximation, the estimated S_2 column density was ~ 1 ML. Thermal desorption of S_3 molecules was not detected (Fig. 4, left panel), while the molecular mass of longer sulfur allotropes (S_n with $n \geq 4$) fell outside of the QMS mass range and could not be monitored. As a result, approximately $\sim 60\%$ of the sulfur consumed during irradiation (corresponding to $\sim 35\%$ of the initial sulfur) could not be tracked at the end of Experiments 1 and 2. The nature of this missing sulfur is discussed in Sect. 4.3.

Based on the reaction scheme proposed in Maity & Kaiser (2013), formation of ^{18}OCS and $^{18}\text{O}^{13}\text{CS}$ molecules in our experiments probably took place through the dissociation of $^{13}\text{C}^{18}\text{O}_2$ and CS_2 molecules, followed by the $\text{CS} + ^{18}\text{O}$ and $^{13}\text{C}^{18}\text{O} + \text{S}$ atom-addition reactions. According to this scheme, the abundance of reactants available for both pathways would in principle be equivalent regardless of the number of dissociated $^{13}\text{C}^{18}\text{O}_2$ and CS_2 molecules during irradiation, because dissociation of these molecules would lead to the same amount of $^{13}\text{C}^{18}\text{O}$ and ^{18}O fragments, and CS and S fragments. In order to estimate the actual relative contribution of both pathways in our experiments, we calculated the area of the ^{18}OCS and $^{18}\text{O}^{13}\text{CS}$ Gaussians in the top left panel of Fig. 2, obtaining a $^{18}\text{OCS}/^{18}\text{O}^{13}\text{CS}$ ratio of ~ 3.7 in Exp. 1 (~ 3.6 in Exp. 2). A similar ratio was obtained from the numerical integration of the m/z 62 and m/z 63 TPD curves shown in the bottom left panel of Fig. 2 (~ 2.4 in Exp. 1 and ~ 2.3 in Exp. 2). Therefore, $\sim 75\%$ of the produced OCS molecules in our experiments were formed through the oxidation of CS ($\text{CS} + \text{O}$) pathway, while the remaining $\sim 25\%$ were formed through the sulfurization of CO ($\text{CO} + \text{S}$) pathway. This suggested that the $\text{CS} + ^{18}\text{O} \rightarrow ^{18}\text{OCS}$ atom-addition reaction was more favorable than the $^{13}\text{C}^{18}\text{O} + \text{S} \rightarrow ^{18}\text{O}^{13}\text{CS}$ reaction.

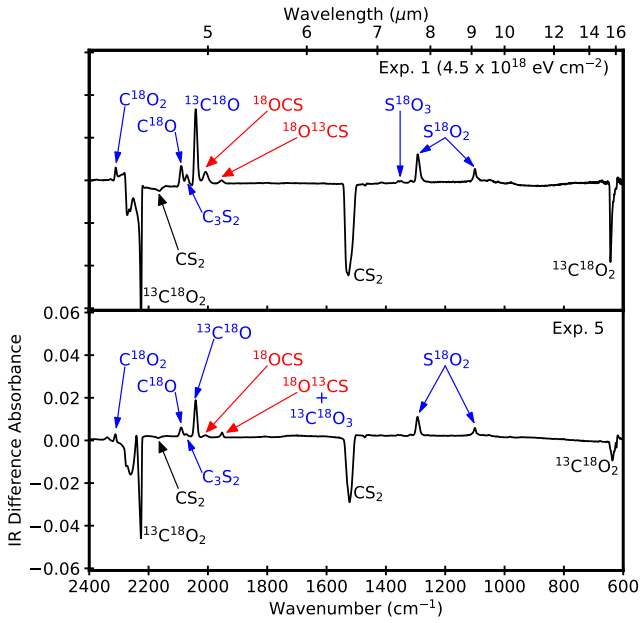


Figure 5. IR difference spectrum obtained upon irradiation of $4.5 \times 10^{18} \text{ eV cm}^{-2}$ with 2 keV electrons (top panel) and VUV photons (bottom panel) of a $^{13}\text{C}^{18}\text{O}_2\text{:CS}_2$ ice sample at 7–10 K in Experiments 1 and 5, respectively. IR band assignments are indicated for the initial ice components (black), and ice chemistry products (blue), including the OCS isotopologs (red).

3.2 VUV photon irradiation of a $^{13}\text{C}^{18}\text{O}_2\text{:CS}_2$ ice sample at 10 K

In order to test whether the nature of the energetic processing could have an effect on the relative contributions of the CO+S and CS+O pathways to the formation of OCS, we irradiated a $^{13}\text{C}^{18}\text{O}_2\text{:CS}_2$ ice sample with VUV photons in Experiments 5 and 6. We note that the initial CS_2 ice abundance in Experiments 5 and 6 was $\sim 7\%$, whereas that of Experiments 1 and 2 was $\sim 12\text{--}15\%$. In addition, the ice irradiation temperature was slightly higher (~ 10 K, the lowest temperature reached in the SPACE CAT experimental setup). In any case, we did not expect these differences to have a significant effect on the relative contributions of the two OCS formation pathways.

The IR difference spectrum in the $2400\text{--}600 \text{ cm}^{-1}$ range after VUV photon irradiation of the ice sample in Exp. 5 is presented in the bottom panel of Fig. 5 (the results were similar in Exp. 6). For comparison, the top panel of Fig. 5 shows the IR difference spectrum of the 2 keV electron irradiated sample in Exp. 1 after a similar irradiated energy fluence. Qualitatively, both spectra looked very similar, but the chemistry seemed to proceed to a larger extent in the electron irradiated ice. Formation of both, ^{18}OCS and $^{18}\text{O}^{13}\text{CS}$ was also detected in the VUV irradiation experiment through the 2009 and 1955 cm^{-1} IR features. However, in this experiment the 1955 cm^{-1} feature presented a contribution from, at least, one additional molecule. While thermal desorption of ^{18}OCS and $^{18}\text{O}^{13}\text{CS}$ was detected above 85 K (Fig. 6, right panel), we observed a decrease in the absorbance of the 1955 cm^{-1} feature between 10 and 80 K (Fig. 6, left panel). This indicated a contribution from a different species that desorbed or dissociated in the 10–80 K temperature range. We speculate that this species could be $^{13}\text{C}^{18}\text{O}_3$. As explained above, formation of CO_3 has been previously reported in VUV irradiation experiments of CO_2 -containing ices (see, e.g., Martín-Doménech et al. 2015; Chen et al. 2015), and the reported position of the corre-

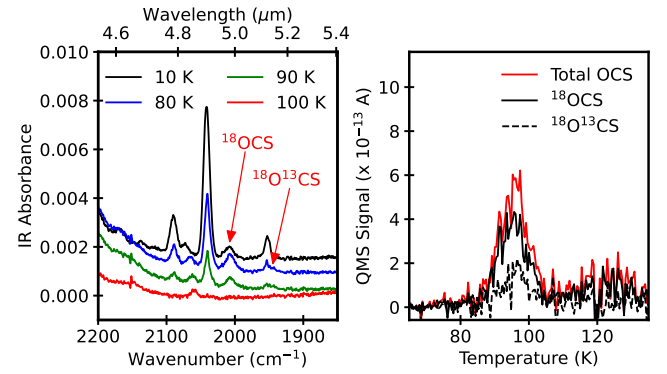


Figure 6. Left: evolution of the IR spectrum during the TPD of the VUV photon irradiated $^{13}\text{C}^{18}\text{O}_2\text{:CS}_2$ ice sample in Exp. 5. The IR spectra during the TPD were collected with a 45° incidence angle. Right: TPD curves corresponding to ^{18}OCS (solid black), and $^{18}\text{O}^{13}\text{CS}$ (dashed black), along with the sum of both signals (red) measured during thermal desorption of the VUV photon irradiated $^{13}\text{C}^{18}\text{O}_2\text{:CS}_2$ ice sample in Exp. 6. Note that the ice sample was not facing the QMS during the TPD in Exp. 5 (so that IR spectra could be collected). This led to TPD curves with a lower signal-to-noise ratio. In any case, the TPD curves were similar in Experiments 5 and 6.

sponding IR feature (2044 cm^{-1}) overlapped with that of OCS (2040 cm^{-1} , Chen et al. 2015). It is thus possible that the IR features of $^{13}\text{C}^{18}\text{O}_3$ and $^{18}\text{O}^{13}\text{CS}$ also overlap. Unfortunately, thermal desorption of CO_3 was not detected in Martín-Doménech et al. (2015), and it was not observed either in Experiments 5 and 6, so we could not confirm the presence of this molecule.

We followed the same procedure as in Sect. 3.1 to calculate the relative contribution of the two OCS formation pathways. To this purpose, we used the numerical integration of the ^{18}OCS and $^{18}\text{O}^{13}\text{CS}$ features in the 80 K IR spectrum (that did not present contributions from any other species), and the m/z 62 and m/z 63 TPD curves, leading to an average $^{18}\text{OCS}/^{18}\text{O}^{13}\text{CS}$ ratio of ~ 3.5 . This indicated that $\sim 78\%$ of the produced OCS was formed through the CS+O pathway, and $\sim 22\%$ through the CO+S pathway, comparable to the values reported in Sect. 3.1 for the electron irradiation experiment. Therefore, the relative contribution of the two OCS formation pathways upon irradiation of $^{13}\text{C}^{18}\text{O}_2\text{:CS}_2$ ice samples did not significantly depend on the nature of the energetic processing.

3.3 2 keV electron irradiation of a $^{13}\text{C}^{18}\text{O}\text{:CS}_2$ ice sample at 7 K

Figure 7 shows the IR difference spectrum in the $2400\text{--}600 \text{ cm}^{-1}$ range obtained upon 2 keV electron irradiation at 7 K of the $^{13}\text{C}^{18}\text{O}\text{:CS}_2$ ice sample in Exp. 7. In this experiment, we observed a lower depletion of CS_2 molecules ($\sim 40\%$ in Exp. 7, compared to $\sim 60\%$ in Experiments 1 and 2), even though the ice thickness, initial CS_2 ice abundance, and irradiated energy fluence were similar to those reported in Sect. 3.1. Therefore, sulfur chemistry proceeded to a lower extent in the irradiated $^{13}\text{C}^{18}\text{O}\text{:CS}_2$ sample compared to a $^{13}\text{C}^{18}\text{O}_2\text{:CS}_2$ ice.

Irradiation of the $^{13}\text{C}^{18}\text{O}\text{:CS}_2$ ice sample led to the formation of $^{13}\text{C}^{18}\text{O}_2$ (with two IR features detected at 2242 and 630 cm^{-1}) and $^{13}\text{C}_3^{18}\text{O}_2$ (with a broad IR feature detected at $\sim 2140 \text{ cm}^{-1}$). The assignment of the $\sim 2140 \text{ cm}^{-1}$ feature to $^{13}\text{C}_3^{18}\text{O}_2$ was based on a preliminary 2 keV electron irradiation experiment of a $\text{CO}\text{:CS}_2$ ice mixture (not shown in this paper) in which the C_3O_2 feature was

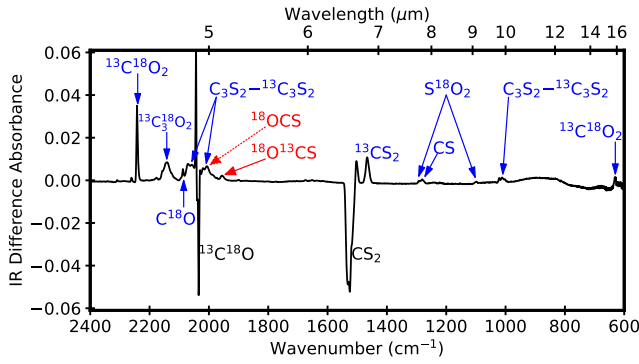


Figure 7. IR difference spectra obtained upon 2 keV electron irradiation of a $^{13}\text{C}^{18}\text{O}:\text{CS}_2$ ice sample at 7 K (Exp. 7). IR band assignments are indicated for the initial ice components (black), and ice chemistry products (blue), including the OCS isotopologs (red).

detected at 2242 cm^{-1} (Sicilia et al. 2012). In addition, formation of C^{18}O was also observed at 2090 cm^{-1} , as in the $^{13}\text{C}^{18}\text{O}_2:\text{CS}_2$ ice samples.

Regarding the S-bearing products, S^{18}O_2 and S^{18}O_3 formation proceeded to a much lower extent in the $^{13}\text{C}^{18}\text{O}:\text{CS}_2$ ice mixture. The integrated absorbance of the S^{18}O_2 1290 cm^{-1} feature was a factor of ~ 50 lower compared to the irradiated $^{13}\text{C}^{18}\text{O}_2:\text{CS}_2$ sample (corresponding to ~ 0.2 ML), while the IR feature corresponding to S^{18}O_3 was not detected. The signal of the S^{18}O_2 TPD curve was also between one and two orders of magnitude lower (see Fig. C2 in Appendix C). This could stem from the lower abundance of ^{18}O atoms in a $^{13}\text{C}^{18}\text{O}:\text{CS}_2$ ice with the same molecular composition than a $^{13}\text{C}^{18}\text{O}_2:\text{CS}_2$ sample (see Table 1). A consequence of the lower absorbance of the 1290 cm^{-1} band was the identification of a small CS IR feature at 1280 cm^{-1} (Bohn et al. 1992; Bahou et al. 2000). This feature could also be present in the spectrum of the irradiated $^{13}\text{C}^{18}\text{O}_2:\text{CS}_2$ sample, but hindered by the more intense S^{18}O_2 band. As for S^{18}O_2 and S^{18}O_3 , formation of S_2 was also hampered in this experiment, and this molecule was not detected during the TPD of the irradiated ice (right panel of Fig. 4).

OCS molecules were formed through both the CS+O and the CO+S pathways also in the $^{13}\text{C}^{18}\text{O}:\text{CS}_2$ ice sample. Unfortunately, the 2099 cm^{-1} ^{18}OCS IR feature overlapped with C_3S_2 isotopolog bands (see below), and only the 1955 cm^{-1} $^{18}\text{O}^{13}\text{CS}$ feature could be unambiguously identified in the IR spectrum. The integrated absorbance of the latter was similar to that measured after irradiation of a $^{13}\text{C}^{18}\text{O}_2:\text{CS}_2$ ice sample. In any case, thermal desorption of both molecules was detected during the TPD of the irradiated ice (Fig. 8, bottom left panel). According to the sum of the m/z 62 and m/z 63 QMS signals, the total number of produced OCS molecules was a factor of ~ 2.5 lower than in the $^{13}\text{C}^{18}\text{O}_2:\text{CS}_2$ experiments, for a total of ~ 0.6 ML of OCS.

On the other hand, formation of C_3S_2 proceeded to a higher extent in the irradiated $^{13}\text{C}^{18}\text{O}:\text{CS}_2$ ice sample, and was the main S-bearing irradiation product in this experiment. The top left panel of Fig. 8 shows a multiple Gaussian fitting of the $2220\text{--}1850\text{ cm}^{-1}$ region of the spectrum. Multiple features with similar absorbances were detected at 2070 (feature a in the Figure), 2055 (b), 2020 (d), 2007 (e), and 1985 cm^{-1} (f), corresponding to C=C antisymmetric stretching of C_3S_2 and the isotopologs SCC^{13}CS , SC^{13}CCS , $\text{S}^{13}\text{C}^{13}\text{CCS}$, and $^{13}\text{C}_3\text{S}_2$, respectively (Bohn et al. 1992). Only the feature corresponding to $\text{S}^{13}\text{CC}^{13}\text{CS}$ was missing, because it overlapped with that of

$^{13}\text{C}^{18}\text{O}$. Four additional features were detected at 1022 , 1012 , 1002 , and 995 cm^{-1} , corresponding to the C=S antisymmetric stretching of the same molecules (Bohn et al. 1992). In addition, thermal desorption of these molecules was detected above 150 K through the C_2S molecular fragments (see bottom left panel of Fig. C2 in Appendix C). The sum of integrated absorbances of the C=C antisymmetric stretching features was ~ 10 times higher¹ than after irradiation of a $^{13}\text{C}^{18}\text{O}_2:\text{CS}_2$ ice sample in Experiments 1 and 2. The estimated column density of C_3S_2 and the different isotopologs was ~ 3.5 ML. The detection of multiple C_3S_2 isotopologs with similar abundances in this experiment contrasted with the formation of only C_3S_2 in the irradiated $^{13}\text{C}^{18}\text{O}_2:\text{CS}_2$ samples, and suggested that ^{13}C atoms coming from $^{13}\text{C}^{18}\text{O}$ played a significant role in the formation of C_3S_2 in this experiment. The interaction of ^{13}C with S was also evidenced by the formation of ~ 1.5 ML of $^{13}\text{CS}_2$ molecules (detected at 1468 cm^{-1}), that was not observed in Experiments 1 and 2. After including ~ 7 ML of S contained in C_3S_2 isotopologs, ~ 3 ML contained in $^{13}\text{CS}_2$, ~ 0.6 ML contained in both OCS isotopologs, and ~ 0.2 ML in S^{18}O_2 molecules, roughly $\sim 45\%$ of the consumed sulfur, corresponding to $\sim 19\%$ of the initial sulfur, was missing at the end of the experiment.

Regarding the contribution of the CO+S and CS+O pathways, only $^{18}\text{O}^{13}\text{CS}$ could be unambiguously identified in the IR spectrum, but thermal desorption of both, $^{18}\text{O}^{13}\text{CS}$ and ^{18}OCS , was detected (as explained above). Therefore, we used the corresponding TPD curves to evaluate the relative contribution of the two OCS formation pathways. While the ice abundance of $^{18}\text{O}^{13}\text{CS}$ was similar in experiments with a CO_2 - and a CO -ice matrix, the TPD curve area corresponding to the ^{18}OCS molecules decreased by a factor of ~ 4 in the irradiated $^{13}\text{C}^{18}\text{O}:\text{CS}_2$ ice compared to a $^{13}\text{C}^{18}\text{O}_2:\text{CS}_2$ sample. As for S^{18}O_2 , the lower ^{18}OCS formation could be due to the lower availability of ^{18}O atoms. According to the integrated m/z 62 and m/z 63 TPD curves, the $^{18}\text{OCS}/^{18}\text{O}^{13}\text{CS}$ ratio was ~ 0.7 . This means that $\sim 40\%$ of the OCS molecules were formed through the CS+O pathway and $\sim 60\%$ were formed through the CO+S pathway. The higher contribution of the CO+S pathway in the $^{13}\text{C}^{18}\text{O}:\text{CS}_2$ ice sample was probably the result of the higher abundance of $^{13}\text{C}^{18}\text{O}$ compared to any other of the required reactants for the formation of OCS (i.e., CS, S, ^{18}O).

3.4 2 keV electron irradiation of $^{13}\text{C}^{18}\text{O}_2:\text{CS}_2$ ice samples at 25 K and 50 K

The IR difference spectra of the $^{13}\text{C}^{18}\text{O}_2:\text{CS}_2$ ice samples irradiated at 25 K and 50 K (Experiments 3 and 4) were similar to those of the samples irradiated at 7 K, and are shown in Fig. A1 of the Appendix A). No significant differences were found in the depletion of $^{13}\text{C}^{18}\text{O}_2$ and CS_2 molecules upon irradiation. The main irradiation product was $^{13}\text{C}^{18}\text{O}$ in all experiments. However, the corresponding IR integrated absorbance was $\sim 35\%$ lower (corresponding to ~ 20 ML less) in the ice sample irradiated at 50 K (Fig. 2, top right panel). A $\sim 55\%$ decrease was also observed for C^{18}O . This could be due to a higher desorption of these molecules during irradiation in the

¹ Note that for this calculation we assumed, as a first approximation, that the integrated absorbance corresponding to the $\text{S}^{13}\text{C}^{13}\text{CS}$ isotopolog (whose feature overlapped with the $^{13}\text{C}^{18}\text{O}$ band) was the same as that of the $\text{S}^{13}\text{C}^{13}\text{CCS}$ isotopolog (feature e in the top left panel of Fig. 8). In addition, we subtracted the expected contribution of the ^{18}OCS IR feature from the sum of C_3S_2 isotopolog integrated absorbances. This contribution was estimated from the $^{18}\text{O}^{13}\text{CS}$ integrated absorbance and the $(m/z\ 62)/(m/z\ 63)$ QMS signal ratio.

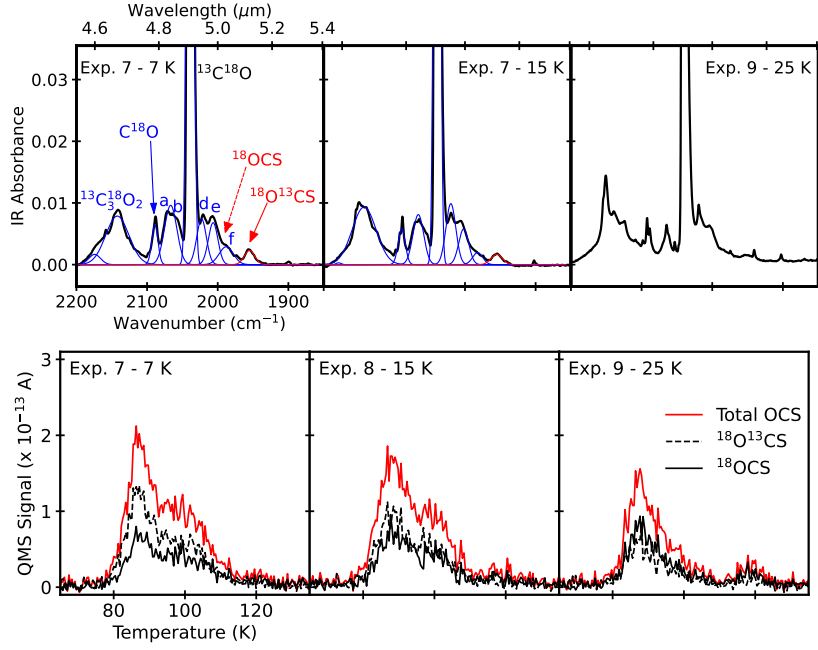


Figure 8. *Top:* Gaussian fitting of the features in the IR spectra of the $^{13}\text{C}^{18}\text{O}:\text{CS}_2$ ice samples irradiated at 7 K (left panel) and 15 K (middle panel). The spectra of the experiment at 25 K could not be fitted (right panel). IR band assignments are indicated for the initial ice components (black), and ice chemistry products (blue), including $^{18}\text{O}^{13}\text{CS}$ (red). The expected position of the ^{18}OCS feature is indicated, but it could not be detected due to overlapping with features corresponding to C_3S_2 isotopologs. The positions of the latter are indicated with letters a–f, corresponding to a) C_3S_2 , b) SCC^{13}CS (these two features were fitted with a single Gaussian), d) SC^{13}CCS , e) $\text{S}^{13}\text{C}^{13}\text{CCS}$, and f) $^{13}\text{C}_3\text{S}_2$. The $\text{S}^{13}\text{CC}^{13}\text{CS}$ feature overlapped with the $^{13}\text{C}^{18}\text{O}$ band and could not be detected either. *Bottom:* TPD curves corresponding to ^{18}OCS (solid black) and $^{18}\text{O}^{13}\text{CS}$ (dashed black), along with the sum of both signals (solid red), measured during thermal desorption of $^{13}\text{C}^{18}\text{O}:\text{CS}_2$ ice samples irradiated at 7 K (left panel), 15 K (middle panel), and 25 K (right panel).

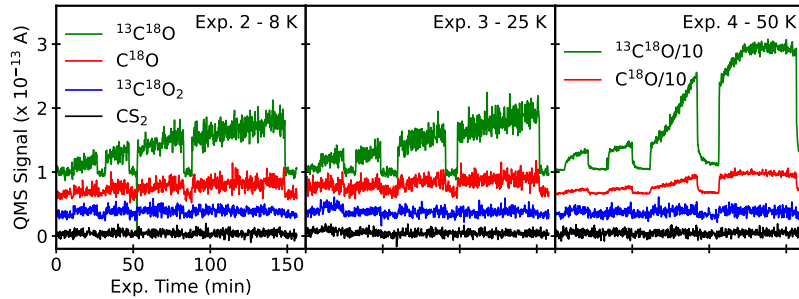


Figure 9. QMS signals corresponding to $^{13}\text{C}^{18}\text{O}_2$ (blue), CS_2 (black), $^{13}\text{C}^{18}\text{O}$ (green), and C^{18}O (red) during irradiation of $^{13}\text{C}^{18}\text{O}_2:\text{CS}_2$ ice samples at 8 K (left panel), 25 K (middle panel) and 50 K (right panel). The signals are offset for clarity. The observed valleys correspond to pauses in the irradiation of the samples. We note that the QMS signals were not monitored during irradiation in Exp. 1.

50 K experiment. Desorption of $^{13}\text{C}^{18}\text{O}$ and C^{18}O molecules (along with a smaller amount of $^{13}\text{C}^{18}\text{O}_2$ molecules) was observed during irradiation of the $^{13}\text{C}^{18}\text{O}_2:\text{CS}_2$ samples at any temperature (Fig. 9). Using the calibration of the QMS described in Sect. 2.5 (as a first approximation, see Appendix B for more information), we estimated that ~ 1 ML of $^{13}\text{C}^{18}\text{O}$ desorbed during irradiation at 7 K and 25 K, while ~ 20 ML desorbed at 50 K. This suggests that the formation of $^{13}\text{C}^{18}\text{O}$ proceeded to the same extent in all experiments, but a higher fraction of the formed molecules desorbed during irradiation in the experiment at 50 K. Similar results were obtained for the C^{18}O desorption.

Regarding the S-bearing products, formation of S^{18}O_2 , S^{18}O_3 , and S_2 proceeded to a similar extent in Experiments 1–4 (see Figures A1 and A2 in Appendix A). On the other hand, the C_3S_2 IR absorbance was $\sim 40\%$ lower in the sample irradiated at 50 K (Fig. 2, top right

panel). We speculate that this decrease could be related to the slight increase in the formation of ^{18}OCS molecules through the $\text{CS} + ^{18}\text{O}$ reaction at 50 K (see below), leading to a lower availability of CS for the formation of C_3S_2 .

The total formation of OCS molecules did not present significant differences in the 7–50 K temperature range. However, the relative contribution of the $\text{CS}+\text{O}$ and $\text{CO}+\text{S}$ pathways slightly changed with the irradiation temperature, according to the corresponding IR features (Fig. 2, top panels) and TPD curves (Fig. 2, bottom panels). The integrated IR absorbances (top panel) and TPD curves (bottom panel) of ^{18}OCS and $^{18}\text{O}^{13}\text{CS}$ (along with the sum of both isotopologs), measured after irradiation of the ice samples at 7, 25, and 50 K, are presented in Fig. 10. The contribution of the $\text{CS}+\text{O}$ pathway (leading to the formation of ^{18}OCS molecules) increased from $\sim 75\%$ at 7 K (Sect. 3.1) to $\sim 85\%$ at 50 K. As observed in Fig. 10,

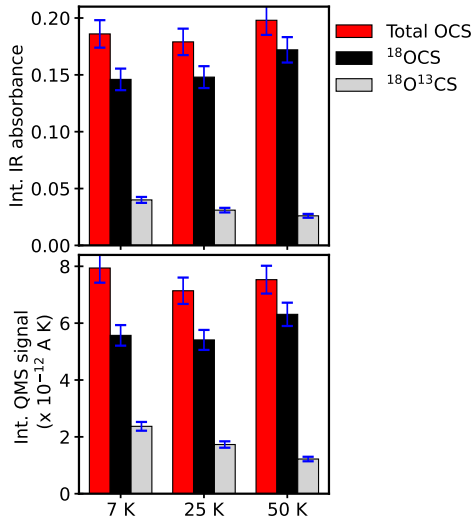


Figure 10. Formation of ^{18}OCS (black) and $^{18}\text{O}^{13}\text{CS}$ (gray), along with the total formation of OCS molecules (red) upon irradiation of $^{13}\text{C}^{18}\text{O}_2:\text{CS}_2$ ice samples at 7–50 K, measured as the integration of the corresponding IR features (top panel) and TPD curves (bottom panel). The values at 7 K are the average of Experiments 1 and 2. A 5% relative experimental uncertainty (blue error bars) was assumed from the differences found between Experiments 1 and 2 (performed under similar conditions).

this increase was mainly due to a gradual decrease in the $^{18}\text{O}^{13}\text{CS}$ formation through the $^{13}\text{C}^{18}\text{O} + \text{S}$ reaction, combined with a small increase in the ^{18}OCS formation at 50 K. We note that the decrease in the $^{18}\text{O}^{13}\text{CS}$ formation could not be due only to the lower $^{13}\text{C}^{18}\text{O}$ ice column density measured in the 50 K experiment, since this decrease was already observed at 25 K (Fig. 10). Therefore, the lower extent of the $^{13}\text{C}^{18}\text{O} + \text{S}$ reaction as the temperature increased should have an additional explanation. This is discussed in Sect. 4.2.

3.5 2 keV electron irradiation of $^{13}\text{C}^{18}\text{O}:\text{CS}_2$ ice samples at 15 K and 25 K

The IR difference spectra of the $^{13}\text{C}^{18}\text{O}:\text{CS}_2$ ice samples irradiated at 15 K and 25 K (Experiments 8 and 9) are shown in Appendix C (Fig. C1, middle and bottom panels, respectively). The CS_2 depletion upon irradiation decreased from $\sim 40\%$ at 7 and 15 K to $\sim 20\%$ at 25 K. This did not affect the formation of $^{13}\text{C}^{18}\text{O}_2$ and $^{13}\text{C}_3^{18}\text{O}_2$, that did not present any significant differences in the 7–25 K temperature range according to their IR absorbances. Regarding the S-bearing products, S^{18}O_2 formation did not seem to drastically change with temperature either (see also Fig. C2 in Appendix C). On the other hand, the formation of C_3S_2 and its isotopologs decreased by a factor of ~ 2 in the experiment at 25 K, according to the numerical integration of the $\sim 1010\text{ cm}^{-1}$ IR features and TPD curves (Fig. C2 in Appendix C). The same decrease was observed for the formation of $^{13}\text{CS}_2$.

The effect of the irradiation temperature on the CS+O and CO+S OCS formation pathways was similar to that observed in the $^{13}\text{C}^{18}\text{O}_2:\text{CS}_2$ mixtures (Sect. 3.4). The integrated TPD curves corresponding to ^{18}OCS and $^{18}\text{O}^{13}\text{CS}$ (along with the sum of both isotopologs) in the experiments at 7, 15, and 25 K are shown in Fig. 11. Formation of ^{18}OCS through the $\text{CS} + ^{18}\text{O}$ reaction did not significantly change with temperature (even though dissociation of CS_2 proceeded to a lower extent at 25 K, as mentioned above). At the same time, the formation of $^{18}\text{O}^{13}\text{CS}$ through the $^{13}\text{C}^{18}\text{O}$

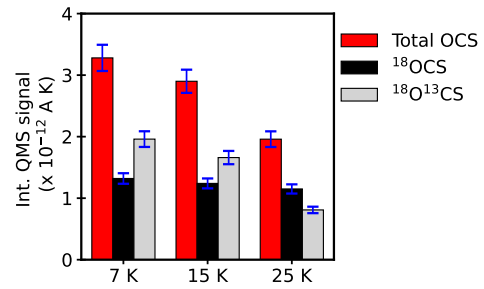


Figure 11. Formation of ^{18}OCS (black) and $^{18}\text{O}^{13}\text{CS}$ (gray), along with the total formation of OCS molecules (red) upon irradiation of $^{13}\text{C}^{18}\text{O}:\text{CS}_2$ ice samples at 7–25 K, measured as the integration of the corresponding TPD curves. The assumed 5% relative experimental uncertainty is indicated as blue error bars.

+ S pathway gradually decreased with temperature. As a result, the relative contribution of the $\text{CS} + ^{18}\text{O}$ pathway to the total formation of OCS increased from $\sim 40\%$ at 7 K to $\sim 60\%$ at 25 K. The observed decrease from 7 to 25 K in the $^{13}\text{C}^{18}\text{O} + \text{S} \rightarrow ^{18}\text{O}^{13}\text{CS}$ reaction was higher in the $^{13}\text{C}^{18}\text{O}:\text{CS}_2$ samples (a factor of ~ 2.5) than in the $^{13}\text{C}^{18}\text{O}_2:\text{CS}_2$ experiments between the same temperatures ($\sim 25\%$). As in the latter experiments, this decrease was probably not due to a lower availability of $^{13}\text{C}^{18}\text{O}$ molecules in the ice at higher temperatures, since formation of $^{13}\text{C}^{18}\text{O}_2$ and $^{13}\text{C}_3^{18}\text{O}_2$ proceeded to the same extent at all temperatures (as explained above). Likewise, the lower dissociation of CS_2 molecules at 25 K (leading to a decrease in the availability of CS and S) could not be the only responsible either, since the decrease was already observed at 15 K (with the same CS_2 dissociation as at 7 K).

3.6 2 keV electron irradiation of $\text{H}_2^{18}\text{O}:\text{CS}_2$ ice samples at 8 K and 50 K

In order to explore the CS+O pathway for OCS formation and its dependence with temperature in a different ice environment, we performed 2 keV electron irradiation experiments of $\text{H}_2^{18}\text{O}:\text{CS}_2$ ice samples at 8 and 50 K (Experiments 10 and 11 in Table 1). In these experiments CS_2 molecules acted as a source of CS and H_2^{18}O as a source of ^{18}O atoms. Therefore, OCS molecules most likely formed through a CS+O pathway, either through the $\text{CS} + ^{18}\text{O}$ atom-addition reaction proposed in Maity & Kaiser (2013) (Eq. 6), and/or through the $\text{CS} + \text{OH}$ neutral-neutral reaction described in Adriaens et al. (2010) (see Sect. 1).

Fig. 12 shows the IR difference spectra in the $2400\text{--}600\text{ cm}^{-1}$ range for the irradiation at 8 K (top panel) and 50 K (bottom panel). In both experiments, $\sim 15\%$ of the initial H_2^{18}O and $\sim 22\%$ of the initial CS_2 molecules were depleted upon irradiation (according to the $\sim 780\text{ cm}^{-1}$ and $\sim 1500\text{ cm}^{-1}$ IR features, respectively). The IR difference spectra revealed the formation of C^{18}O and C^{18}O_2 , with IR features detected at 2090 cm^{-1} and 2310 cm^{-1} (respectively). As in the $^{13}\text{C}^{18}\text{O}_2:\text{CS}_2$ and $^{13}\text{C}^{18}\text{O}:\text{CS}_2$ experiments (Sect. 3.1), formation of C^{18}O could have taken place through addition reactions to C atoms from completely dissociated CS_2 molecules, and/or through dissociation of previously produced ^{18}OCS molecules.

On the other hand, three S-bearing products were detected upon irradiation of the $\text{H}_2^{18}\text{O}:\text{CS}_2$ ice samples. Formation of S^{18}O_2 was detected in the IR difference spectra at 1290 cm^{-1} (Fig. 12), and during the TPD of the irradiated ice samples (Fig. D1 in Appendix D). The estimated ice column density was $\sim 0.2\text{ ML}$ at 8 K, and a

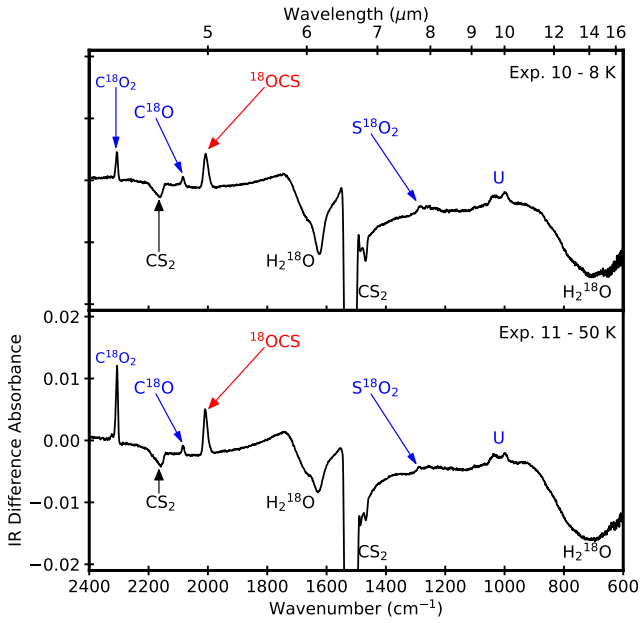


Figure 12. IR difference spectra obtained upon 2 keV electron irradiation of a $\text{H}_2^{18}\text{O}:\text{CS}_2$ ice sample at 8 K (Exp. 10, top panel) and 50 K (Exp. 11, bottom panel). IR band assignments are indicated for the initial ice components (black), and ice chemistry products (blue), including ^{18}OCS (red). The unidentified features (U) could be related to structural changes in the H_2^{18}O ice matrix. Further experiments beyond the scope of this paper would be required to confirm this scenario.

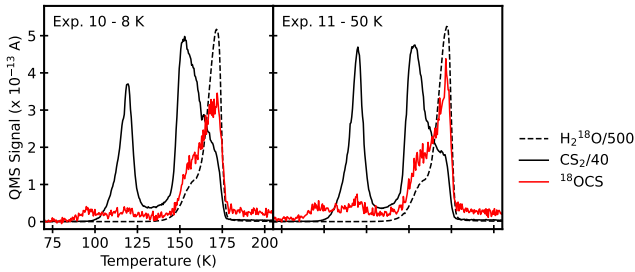


Figure 13. TPD curves corresponding to the remaining H_2^{18}O (dashed black) and CS_2 (solid black), and the produced ^{18}OCS (solid red), measured during thermal desorption of the $\text{H}_2^{18}\text{O}:\text{CS}_2$ ice samples irradiated at 8 K (Exp. 10, left panel) and 50 K (Exp. 11, right panel).

factor of 2 lower at 50 K, representing less than 1% of the consumed S during irradiation. We also tentatively detected co-desorption of less than 1 ML of S_2 molecules with H_2^{18}O during the TPD of the irradiated ice samples (Fig. D1 in Appendix D). The main detected S-bearing product was ^{18}OCS , with an IR feature at 2009 cm^{-1} (Fig. 12). The corresponding TPD curves are shown in Fig. 13. We note that while a small fraction of the ^{18}OCS molecules desorbed at $\sim 95\text{ K}$ or co-desorbed with CS_2 at $\sim 120\text{ K}$, most of the produced ^{18}OCS in these experiments was entrapped in the H_2^{18}O ice matrix and co-desorbed with this species at $\sim 170\text{ K}$. According to the integrated IR absorbance, the ^{18}OCS ice column density was $\sim 1\text{ ML}$ in the experiment at 8 K (representing $\sim 2\%$ of the depleted sulfur upon irradiation), and a $\sim 15\%$ higher at 50 K. Therefore, the vast majority

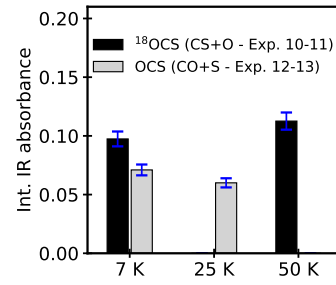


Figure 14. Formation of ^{18}OCS (black) upon irradiation of $\text{H}_2^{18}\text{O}:\text{CS}_2$ ice samples, and OCS (gray) upon irradiation of $\text{CO}:\text{H}_2\text{S}$ mixtures at 7–50 K, measured as the integration of the corresponding IR features. The 5% relative experimental uncertainty is indicated as blue error bars.

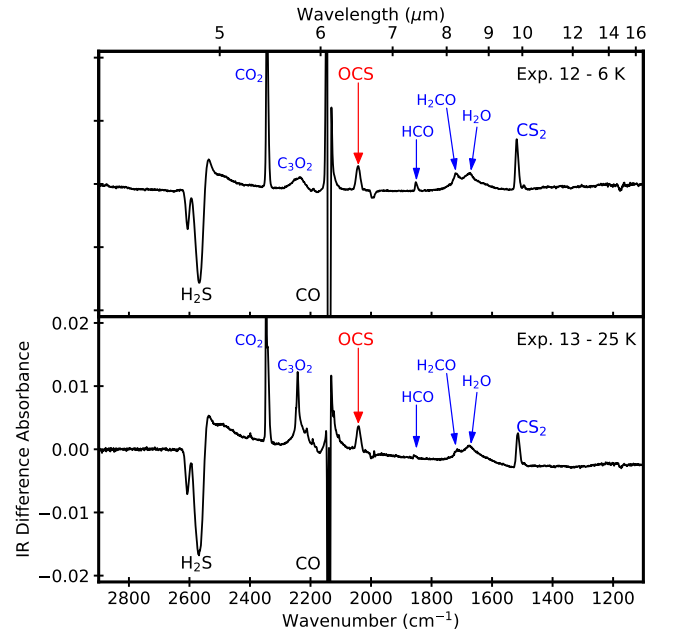


Figure 15. IR difference spectra obtained upon 2 keV electron irradiation of a $\text{CO}:\text{H}_2\text{S}$ ice sample at 6 K (Exp. 12, top panel) and 25 K (Exp. 13, bottom panel). IR band assignments are indicated for the initial ice components (black), and ice chemistry products (blue), including OCS (red).

($\sim 95\%$) of the depleted sulfur could not be tracked at the end of Experiments 10 and 11.

Fig. 14 shows the integrated ^{18}OCS IR absorbances. As mentioned above, the ^{18}OCS column density was $\sim 15\%$ higher at 50 K. A $\sim 15\%$ increase was also observed in the ^{18}OCS formation through the $\text{CS}+\text{O}$ pathway upon irradiation of a $^{13}\text{C}^{18}\text{O}_2:\text{CS}_2$ sample at 50 K, compared to irradiation at lower temperatures (Fig. 10).

3.7 2 keV electron irradiation of $\text{CO}:\text{H}_2\text{S}$ ice samples at 6 and 25 K

Following the results presented in Sect. 3.6, we also studied the evolution with temperature of the OCS formation through the $\text{CO}+\text{S}$ pathway in a different ice environment. To this purpose, Experiments 12 and 13 in Table 1 consisted in the 2 keV electron irradiation of $\text{CO}:\text{H}_2\text{S}$ ice samples at 6 and 25 K, respectively. In those experiments, OCS molecules probably formed through the $\text{CO} + \text{S}$ atom-addition

reaction (Eq. 1), and/or through the CO + HS neutral-neutral reaction (Equations 2, 3, and 4).

As explained in Sect. 1, the energetic processing of CO:H₂S ice mixtures has been previously studied in Ferrante et al. (2008), Garozzo et al. (2010), and Chen et al. (2015). A thorough analysis of the chemistry in Experiments 12 and 13 was thus beyond the scope of this paper. Our focus was instead in the dependence of OCS formation with temperature, that had not been evaluated in the above-mentioned works. Figure 15 shows the IR difference spectra in the 2900–1100 cm⁻¹ range for the experiments at 6 K (top panel) and 25 K (bottom panel), with OCS molecules detected at ~2040 cm⁻¹. The integrated OCS IR absorbances are shown in Fig. 14. We observed a ~15% decrease in the OCS formation at 25 K compared to that at 6 K. Even though this decrease was lower than the ~25% decrease observed for the ¹³C¹⁸O + S → ¹⁸O¹³CS reaction in the ¹³C¹⁸O₂:CS₂ experiments (Fig. 10), and the ~2.5 decrease observed in the ¹³C¹⁸O:CS₂ experiments (Fig. 11), it was in line with the trend observed in those experiments.

4 DISCUSSION

4.1 Relative contribution of the CO+S and CS+O pathways to the formation of OCS in interstellar ices

The experimental results presented in Sections 3.1–3.3 suggest that the CS + ¹⁸O → ¹⁸OCS atom-addition reaction is more favorable than the ¹³C¹⁸O + S → ¹⁸O¹³CS reaction. In the irradiated ¹³C¹⁸O₂:CS₂ ice samples (where both pathways were expected to equally contribute to the formation of OCS), up to ~75% of the detected OCS molecules were formed through the CS+O pathway (Sections 3.1 and 3.2). At the same time, in an irradiated ¹³C¹⁸O:CS₂ ice sample (with a much higher abundance of ¹³C¹⁸O compared to the other reactants), the relative contribution of both pathways was close to 50% (Sect 3.3).

According to the literature, photodissociation of CO₂ and CS₂ molecules with VUV photons mainly leads to CO(X¹Σ_g⁺) + O(¹D), and CS(a³Π/A¹Π) + S(³P) (respectively, see Slanger & Black 1971; Okabe 1978; Zhu & Gordon 1990). As a result, in the VUV-photon irradiated ¹³C¹⁸O₂:CS₂ ice samples (Experiments 5 and 6 in Table 1), the reactants of the CS + ¹⁸O atom-addition reaction would be in electronic excited states (i.e., more reactive), while those of the ¹³C¹⁸O + S reaction would be in the electronic ground state. On the other hand, Zhu et al. (2018) and Maity & Kaiser (2013) reported that 5 keV electron irradiation of CO₂ and CS₂ ice molecules led to the formation of CO + O(¹D/³P), and CS(X¹Σ_g⁺) + S(³P), respectively. The same dissociation channels could be expected upon irradiation with 2 keV electrons (Experiments 1–4 in Table 1). Despite the different reported dissociation channels following VUV photon and keV electron irradiation of CO₂ and CS₂ molecules, the contribution of the CS+O and CO+S pathways to the formation of OCS molecules was very similar upon irradiation of ¹³C¹⁸O₂:CS₂ ice samples with 2 keV electrons and VUV photons (Sections 3.1 and 3.2). This suggests that the electronic state of the reactants might not have played a significant role in the formation of OCS in the experiments reported in this work.

Independently from the dissociation channels of ¹³C¹⁸O₂, ¹³C¹⁸O, and CS₂, theoretical calculations reported in Adriaens et al. (2010) indicated that oxidation of CS is more energetically favorable than sulfurization of CO. Even though Adriaens et al. (2010) studied the CO + S/HS and CS + O/OH reactions on a coronene surface instead that in the bulk of an ice mantle (see Sect. 1), some of

their findings can be used to interpret the results of this work. Three types of surface reactions were studied in Adriaens et al. (2010): the Langmuir-Hinshelwood mechanism (LH, where both reactants are in thermal equilibrium with the surface, i.e., in the vibrational ground state), the hot atom mechanism (HA, where at least one of the reactants is thermally activated), and the Eley-Rideal mechanism (ER, where one of the reactants is in the gas phase). While the latter is not relevant to ice bulk chemistry, the first two mechanisms could be comparable to the processes taking place in ice mantles. According to these theoretical calculations, the addition reaction of a S atom in the ground electronic state to CO (CO + S(³P)) can only take place to a significant extent in the ISM if one of the reactants is thermally activated (i.e., only the reaction through the HA mechanism is exothermic). In case the S atom is in the first electronic excited state, the CO + S(¹D) reaction would be more exothermic than the CO + S(³P) reaction, and could in principle proceed through both, the LH and the HA mechanisms. However, S(¹D) must also be thermally activated for the reaction to proceed, because otherwise it would chemisorb on the coronene surface, and the reaction would be strongly activated. On the other hand, the CS + O(³P/¹D) reactions were more exothermic than the equivalent CO + S ones. In addition, the calculated CS adsorption energy was more than two times higher than that of CO. This would reduce the efficiency of the CS desorption, leading to higher reaction rates. More importantly, the addition reaction of an O atom to CS led to the formation of a van der Waals complex that significantly reduced the activation barriers of these reactions, that could be easily overcome in the ISM (Adriaens et al. 2010). As a result, the CS + O(³P) reaction could take place in the ISM without thermal activation of the reactants, unlike the CO + S(³P) reaction. Therefore, previous theoretical calculations predicted that formation of OCS through the CS+O pathway would be more favorable than through the CO+S pathway. The results presented in this work thus represent the first experimental evidence that oxidation of CS would be preferred over sulfurization of CO in interstellar ice mantles.

4.2 The effect of ice temperature on the CO+S and CS+O OCS formation pathways

The results presented in Sections 3.4 and 3.5 indicated that, in ¹³C¹⁸O₂:CS₂ and ¹³C¹⁸O:CS₂ ice samples, the OCS formation through the ¹³C¹⁸O + S reaction gradually took place to a lower extent as the ice temperature increased in the 7–50 K range. At the same time, formation through the CS + ¹⁸O was slightly higher at 50 K. Similar trends were observed in H₂¹⁸O:CS₂ and CO:H₂S ice samples, where the neutral-radical reactions CS + ¹⁸OH and CO + HS could also contribute to the formation of OCS (Sections 3.6 and 3.7, respectively).

As mentioned in Sections 3.4 and 3.5, the gradual decrease observed for the ¹³C¹⁸O + S reaction was probably not related to a lower availability of ¹³C¹⁸O molecules in the ice. In the ¹³C¹⁸O₂:CS₂ experiments, this decrease was observed already at 25 K, with the same measured ¹³C¹⁸O ice column density as at 7 K (Sect. 3.4). In the ¹³C¹⁸O:CS₂ experiments, the formation of other products derived from ¹³C¹⁸O, such as ¹³C¹⁸O₂ and ¹³C₃¹⁸O₂, remained constant at all temperatures (Sect. 3.5). We speculate that this decrease could instead be due to a lower availability of S atoms at higher temperatures. This could be caused, for example, by a subtle increase in the efficiency of sulfur allotrope formation (see Sect. 4.3). Unfortunately, we could not confirm this scenario with our experimental results because the observed decrease, while significant in terms of OCS

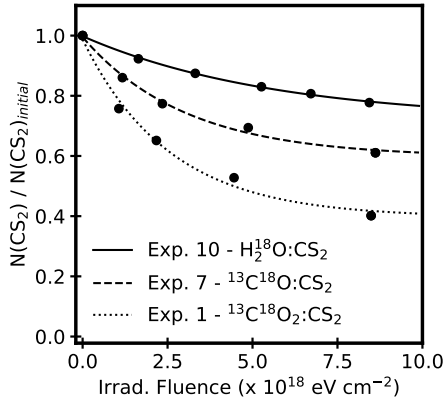


Figure 16. Evolution of the CS₂ column density (normalized to the initial CS₂ column density, black circles) with the irradiated fluence in H₂¹⁸O:CS₂ (Exp. 10, solid line), ¹³C¹⁸O:CS₂ (Exp. 7, dashed line), and ¹³C¹⁸O₂:CS₂ (Exp. 1, dotted line) ice samples. Black lines correspond to pseudo-first order fits.

formation, represented a very small change in the global balance of the sulfur chemistry (due to the small conversion from CS₂ to OCS in these experiments). This possibility will be further explored in a follow-up paper using theoretical simulations to model the irradiation experiments presented in this work (Sipillä et al. in prep.).

4.3 Sulfur chemistry in CS₂-bearing ices

As explained in Sect. 1, Experiments 1–11 in Table 1 also allowed us to explore the sulfur chemistry of ices containing CS₂ molecules in realistic environments, namely, H₂O-, CO-, and CO₂-rich ice matrices. Fig. 16 shows the evolution of the CS₂ ice column density with respect to the initial value during 2 keV electron irradiation of H₂¹⁸O:CS₂, ¹³C¹⁸O:CS₂, and ¹³C¹⁸O₂:CS₂ ice samples at 7–8 K (corresponding to Experiments 10, 7, and 1 in Table 1, respectively). In all experiments, the depletion of CS₂ after irradiation was close to the steady state value. Dissociation of CS₂ molecules led to the formation of several S-bearing products. Figure 17 shows the distribution of S atoms after irradiation in these experiments, including the remaining CS₂ molecules and the different S-bearing products. Figures 16 and 17 indicate that sulfur chemistry proceeded to a higher extent in the ¹³C¹⁸O₂:CS₂ ice samples, where ~60% of the initial CS₂ molecules were transformed into other products, compared to ~40% in ¹³C¹⁸O:CS₂ ices, and ~20% in H₂¹⁸O:CS₂ samples.

The most abundant S-bearing product detected in the irradiated ¹³C¹⁸O₂:CS₂ ice sample was S¹⁸O₂, that accounted for ~26% of the sulfur participating in the ice chemistry (i.e., not present in CS₂ molecules after irradiation), while OCS molecules represented ~5% of this fraction of sulfur. Interestingly, ~60% of the sulfur atoms involved in the chemistry could not be detected at the end of the experiment (see right panel of Fig. 17). A similar problem was encountered in Chen et al. (2015), with detected S-bearing products accounting for less than 20% of the initial sulfur content after photolysis of CO:H₂S and CO₂:H₂S ices. Similarly, Mifsud et al. (2022) reported that 25–45% of the initial sulfur was not observable after electron irradiation of amorphous and crystalline H₂S and SO₂ ice samples. As in Chen et al. (2015) and Mifsud et al. (2022), we speculate that the missing sulfur in our experiments could be contained in long sulfur allotropes (S_n) undetectable with our instruments. Formation of S-polymers from S-bearing species was first suggested in Barnes et al. (1974). Unfortunately, these molecules are not usually active in

the IR, and their detection is elusive. Muñoz Caro (2002) was able to detect S-polymers in the room-temperature residues resulting from the UV irradiation of H₂S ice samples using chromatographic techniques. Formation of (semi-)refractory sulfur chains in H₂S-bearing ices, including sulfur allotropes and polysulfides (H₂S_x), has more recently been studied in Cazaux et al. (2022) and Carrascosa et al. (2024). In particular, Carrascosa et al. (2024) reported the tentative detection of the sulfur allotropes S₂ and S₈ during the TPD of an irradiated H₂O:H₂S ice at 10 K. In our experiments, thermal desorption of S₂ was detected at 110–115 K (Sect. 3.1). Unfortunately, the molecular mass of sulfur allotropes with 4 or more atoms fell outside of the QMS mass range. In any case, S₈ could have been detected through the S₂⁺ fragment, but the desorption temperature reported in Carrascosa et al. (2024) (>260 K) was beyond the temperature range of our TPD.

The fraction of missing sulfur in our experiments was somewhat lower (~45%) in the irradiated ¹³C¹⁸O:CS₂ ice (where thermal desorption of S₂ was not detected, Sect. 3.3). In this case, C₃S₂ and its isotopologs were the most abundant detected S-bearing product, accounting for ~34% of the sulfur contained in products, while OCS molecules represented ~3% of this sulfur. On the other hand, OCS was the most abundant S-bearing product detected in irradiated H₂¹⁸O:CS₂ samples, representing ~2% of the sulfur participating in the chemistry. However, most of this sulfur (~95%) could not be detected after irradiation (left panel of Fig. 17). As in the ¹³C¹⁸O₂:CS₂ experiments, we speculate that the missing sulfur in these experiments could be contained in long, undetectable sulfur chains. We note that, in the literature, irradiation of H₂O:H₂S ice samples mainly led to the formation of polysulfides (H₂S_x) and sulfur allotropes, suggesting that reactions between S-bearing reactants could have dominated the chemistry over reactions with H₂O molecules and OH radicals (Jiménez-Escobar & Muñoz Caro 2011; Carrascosa et al. 2024). A similar scenario could have occurred in the H₂¹⁸O:CS₂ experiments presented in this work.

4.4 Astrophysical implications

The experimental results presented in this work indicate that, in irradiated ¹³C¹⁸O₂:CS₂ ice samples at 7–8 K, the contribution of the CS+O pathway to the formation of OCS was ~3 times higher than the contribution of the CO+S pathway. This value increased up to a factor of ~6 at 50 K. In interstellar ice mantles, the relative contribution of the two pathways will depend not only on the relative efficiency of the reactions, but also on the availability of the reactants and, in particular, on the CO/CS and O/S abundance ratios. In our experiments, dissociation of the ¹³C¹⁸O₂ and CS₂ molecules led to the same ¹³C¹⁸O/CS and atomic ¹⁸O/S ratios. In the ISM, the gas-phase CO/CS ratio is ~2 × 10⁴ (Laas & Caselli 2019, and references therein), which would favor formation of OCS through the CO+S pathway if the same ratio was found in interstellar ices. Even though CS is yet to be detected in interstellar ices, it has been observed in comets (whose composition is expected to resemble that of interstellar ices), with much lower CO/CS ratios (~10–100) than those measured in the gas phase (Bockelée-Morvan & Biver 2017). In addition, the estimated CS binding energy is higher than that of CO (see, e.g., Wakelam et al. 2017). As a result, ice mantles in warm interstellar environments could present even lower CO/CS ratios. Under these circumstances, the more favorable CS+O pathway could play a significant role in the formation of OCS. On the other hand, the volatile O/S ratio in the solid phase is not fully constrained. If a large fraction of S is locked in (semi-)refractory form (as discussed in Millar & Herbst 1990; Ruffle et al. 1999; Vidal et al. 2017;

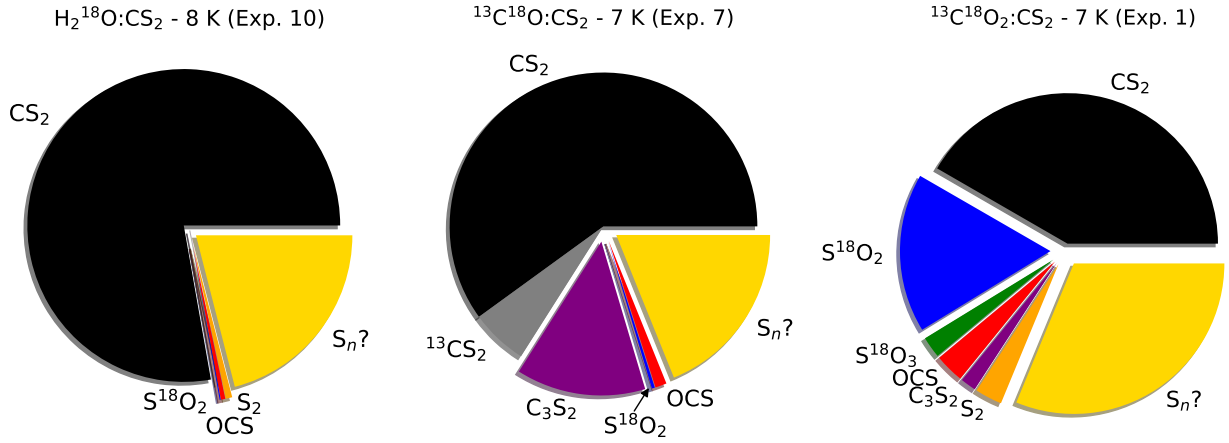


Figure 17. Distribution of the initial sulfur in the ice across the remaining CS_2 molecules and the detected S-bearing products after 2 keV electron irradiation of $\text{H}_2^{18}\text{O}:\text{CS}_2$ (Exp. 10, left panel), $^{13}\text{C}^{18}\text{O}:\text{CS}_2$ (Exp. 7, middle panel), and $^{13}\text{C}^{18}\text{O}_2:\text{CS}_2$ (Exp. 1, right panel) ice samples at 7–8 K. The OCS and C_3S_2 slabs include all detected isotopologs of each species.

Drozdovskaya et al. 2018; Kama et al. 2019; Fuente et al. 2019; Rivière-Marichalar et al. 2020; Fuente et al. 2023), that could also favor a larger contribution of the CS+O pathway.

In an attempt to shed light on the molecular environment and formation history of OCS in interstellar ices, Boogert et al. (2022) recently evaluated the observed ice column density correlations between OCS and different species. However, the results were not conclusive. The best correlations were found with OCN^- and CH_3OH . This would suggest that formation of OCS takes place in the apolar, CO-rich ice layer, thus probably through a CO+S pathway. However, no correlation was found between OCS and the apolar component of CO. Moreover, even though a somewhat poorer correlation was found with the polar component of CO (that would be present in the H_2O -rich ice layer), the OCS ice column density did not correlate with H_2O either. In our experiments, OCS formation was readily observed in a H_2O -rich, a CO-rich, and a CO_2 -rich ice environment, with conversions on the same order of magnitude in all cases (representing $\sim 2\text{--}5\%$ of the sulfur coming from dissociated CS_2 molecules, Sect. 4.3). In contrast, other detected S-bearing products presented differences in their conversions of up to an order of magnitude across different ice environments. Following the results presented in this work, formation of OCS has now been observed in the laboratory upon energetic processing of virtually any ice mixture containing O, C, and S ($\text{CO}:\text{H}_2\text{S}$, $\text{CO}_2:\text{H}_2\text{S}$, $\text{CO}:\text{SO}_2$, $\text{CO}_2:\text{SO}_2$, $\text{CO}:\text{CS}_2$, $\text{CO}_2:\text{CS}_2$, $\text{H}_2\text{O}:\text{CS}_2$, $\text{O}_2:\text{CS}_2$, see Ferrante et al. 2008; Garozzo et al. 2010; Maity & Kaiser 2013; Chen et al. 2015, and this work). The robust formation of this molecule in different ice environments may explain its ubiquitous detection in interstellar ice mantles (see, e.g., Boogert et al. 2022).

Finally, the experiments presented in this work suggest that energetic processing of CS_2 -bearing ices might lead to the formation of sulfur allotropes. These molecules are one of the potential carriers proposed in the literature to harbor the missing sulfur in dense interstellar regions (see, e.g., Wakelam et al. 2004; Fuente et al. 2019; Shingledecker et al. 2020; Cazaux et al. 2022). Fuente et al. (2019) reported that depletion of sulfur by one order of magnitude is already observed in translucent clouds, where sulfur atoms or ions would be incorporated onto the surface of dust grains. According to the theoretical model presented in Cazaux et al. (2022), this depleted sulfur would preferentially form long S-chains. Sulfur is further depleted in the interior of dense clouds, where formation of S-polymers could

also take place upon energetic processing of S-bearing ice mantles. Thus far, formation of (semi-)refractory sulfur chains had been observed in irradiated ices containing H_2S (see, e.g., Muñoz Caro 2002; Garozzo et al. 2010; Jiménez-Escobar & Muñoz Caro 2011; Chen et al. 2015; Cazaux et al. 2022; Carrascosa et al. 2024) and, likely, SO_2 (Mifsud et al. 2022). Therefore, the results presented in this work could represent an additional evidence that formation of sulfur allotropes is common in energetically processed S-bearing ice mantles. Further experiments beyond the scope of this paper are needed in order to confirm and characterize the formation of sulfur allotropes in CS_2 -bearing ices.

5 CONCLUSIONS

In this work, we have simulated the energetic processing of $^{13}\text{C}^{18}\text{O}_2$ -, $^{13}\text{C}^{18}\text{O}$ -, and H_2^{18}O -rich, CS_2 -bearing ice samples at temperatures relevant to the dense ISM (7–50 K).

- Sulfur chemistry proceeded to a larger extent in $^{13}\text{C}^{18}\text{O}_2:\text{CS}_2$ ices, where depletion of the initial CS_2 molecules was up to 3 times higher than in $^{13}\text{C}^{18}\text{O}:\text{CS}_2$ and $\text{H}_2^{18}\text{O}:\text{CS}_2$ samples.
- Dissociation of CS_2 molecules led to the formation of a variety of S-bearing products, including S^{18}O_2 , C_3S_2 , OCS, and S_2 . Formation of OCS has been readily observed in the laboratory upon energetic processing of ice samples with different S-carriers and compositions, which may explain its ubiquitous detection in interstellar ices.
 - In $^{13}\text{C}^{18}\text{O}_2:\text{CS}_2$ ice samples irradiated at 7 K (with the same $^{13}\text{C}^{18}\text{O}/\text{CS}$ and atomic $^{18}\text{O}/\text{S}$ ratios), the CS+O pathway was responsible for the formation of $\sim 75\%$ of the OCS molecules, while the CO+S pathway only contributed to $\sim 25\%$ of the total OCS formation. At the same time, in irradiated $^{13}\text{C}^{18}\text{O}:\text{CS}_2$ ice samples (with a much higher abundance of $^{13}\text{C}^{18}\text{O}$ compared to the other reactants), the relative contribution of both pathways was close to 50%. The measured relative contribution did not depend on the irradiation source (2 keV electrons or VUV photons).
 - In addition, the contribution of the CS+O pathway increased at higher temperatures, due to a combination of a slight increase in the formation of OCS through the CS+O pathway at ~ 50 K, and a gradual decrease of the CO+S pathway in the 7–50 K temperature range. The latter could be due to a lower availability of S atoms to

participate in the formation of OCS at higher temperatures, perhaps due to a subtle increase in the efficiency of competing reactions, such as the formation of sulfur allotropes.

- These experimental results thus suggested that the CS+O pathway was more favorable (as theoretically predicted in the literature), and could play a role in OCS formation in interstellar ices, especially in warm regions where CO would preferentially be in the gas phase.

- More than 50% of the sulfur atoms involved in the ice chemistry were not detected at the end of the experiments, and could be contained in long, undetectable sulfur allotropes. These molecules are one of the potential S-carriers in the dense ISM. These results could represent an additional evidence that formation of sulfur allotropes is common in energetically processed S-bearing ice mantles. Further experiments are needed in order to confirm and characterize the formation of sulfur allotropes in CS₂-bearing ices.

ACKNOWLEDGEMENTS

The project leading to these results has received funding from “la Caixa” Foundation, under agreement LCF/BQ/PI22/11910030. This work was also supported by a grant from the Simons Foundation (686302, KÖ) and an award from the Simons Foundation (321183FY19, KÖ). GMMC and HC received funding from project PID2020-118974GB-C21 by the Spanish Ministry of Science and Innovation. AF has received funding from the European Research Council (ERC) under the European Union’s Horizon Europe research and innovation programme ERC-AdG-2022 (GA No. 101096293) AF also thanks project PID2022-137980NB-I00 funded by the Spanish Ministry of Science and Innovation/State Agency of Research MCIN/AEI/ 10.13039/501100011033 and by “ERDF A way of making Europe”.

DATA AVAILABILITY

The data underlying this article are available in the zenodo repository at <https://zenodo.org>, and can be accessed with DOI: 10.5281/zenodo.13908992.

REFERENCES

Adriaens D.A., Goumans T.P.M., Catlow C.R.A., Brown W.A., 2010, *JPhCh*, 114, 1892
 el Akel M., Kristensen L.E., Le Gal R., van der Walt S.J., Pitts R.L., Dulieu F., 2022, *A&A*, 659, A100
 Asplund M., Grevesse N., Sauval A.J., Scott P., 2009, *ARA&A*, 47, 1, 481
 Bahou M., Lee Y.-C., Lee Y.-P., 2000, *JChS*, 122, 661
 Barnes A.J., Hallam H.E., Howels J.D.R., 1974, *JMoSt*, 23, 463
 Bennett C.J., Jamieson C., Mebel A.M., Kaiser R.I., 2004, *PCCP*, 6, 735
 Bergner J.B., Öberg K.I., Rajappan, M., 2017, *ApJ*, 845, 1, id.29
 Bockelée-Morvan D., Biver N., 2017, *Philosophical Transactions of the Royal Society A*, 375, 2097, id.20160252
 Bohn R.B., Hannachi Y., Andrews L., 1992, *JChS*, 114, 6452
 Boogert A.C.A., Brewer K., Brittain A., Emerson K.S., 2022, *ApJ*, 941, 1, id. 32
 Calmonte U. et al., 2016, *MNRAS*, 462, 1, S253
 Carrascosa H., Muñoz Caro G.M., Martín-Doménech R., Cazaux S., Chen Y.-J., Fuente A., 2024, *MNRAS*, *accepted*
 Cazaux S., Carrascosa H., Muñoz Caro G.M., Caselli P., Fuente A., Navarro-Almáida D., Rivière-Marichalar P., 2022, *A&A*, 657, A100
 Chen Y.-J. et al., 2015, *ApJ*, 798, 2, id.80
 Cruz-Díaz G.A., Muñoz Caro G.M., Chen Y.-J., Yih T.-S., 2014, *A&A*, 562, A120

d’Hendecourt L. B., Allamandola L. J., 1986, *A&AS*, 64, 453
 Drouin D., Couture A.R., Joly D., Tastet X., Aimez V., Gauvin R., 2007, *Scanning*, 29, 3, 92
 Drozdovskaya M.N. et al., 2018, *MNRAS*, 476, 4, 4949
 Ferrante R.F., Moore M.H., Spiliotis M.M., Hudson R.L., 2008, *ApJ*, 684, 2, 1210
 Fuente A. et al., 2019, *A&A*, 624, A105
 Fuente A. et al., 2023, *A&A*, 670, A114
 Garozzo M., Fulvio D., Kanuchova Z., Palumbo M.E., Strazzulla G., 2010, *A&A*, 509, A67
 Gerakines P.A., Moore M.H., 2001, *Icarus*, 154, 2, 372
 Gerakines P.A., Schutte W.A., Greenberg J.M., van Dishoeck E.F., 1995, *A&A*, 296, 810
 Hovington P., Drouin D., Gauvin R., 1997, *Scanning*, 19, 1
 Jiménez-Escobar A., Muñoz Caro G.M., 2011, *A&A*, 536, A91
 Jones B.M., Bennet C.J., Kaiser R.I., 2011, *ApJ*, 734, 78
 Jones P.R., Taube H., 1973, *JPhCh*, 77, 1007
 Kama M., Shorttle O., Jermyn A.S., Folsom C.P., Furuya K., Bergin E.A., Walsh C., Keller L., 2019, *ApJ*, 885, 2, id. 114
 Laas J., Caselli P., 2019, *A&A*, 624, A108
 Lauck T., Karssemeijer L., Shulenberg K., Rajappan M., Öberg K.I., Cuppen H.M., 2015, *ApJ*, 801, 2, id.118
 Maity S., Kaiser R.I., 2013, *ApJ*, 773, 2, id. 184
 Majkowsky R.F., Blint R.J., Hill J.C., 1978, *ApOpt*, 17, 975
 Maksyutenko P., Martín-Doménech R., Piacentino E.L., Öberg K.I., Rajappan, M., 2022, *ApJ*, 940, 2, id.113
 Martín-Doménech R., DelFranco A., Öberg K.I., Rajappan, M., 2024, *ApJ*, 962, 107
 Martín-Doménech R., Manzano-Santamaría J., Muñoz Caro G.M., Cruz-Díaz G.A., Chen Y.-J., Herrero V.J., Tanarro I., 2015, *A&A*, 584, A14
 Martín-Doménech R., Öberg K.I., Rajappan, M., 2020, *ApJ*, 894, 2, id.98
 McClure M.K. et al., 2023, *NatAs*, 7, 431
 Mifsud D.V. et al., 2022, *Front. Chem.*, 10, 1003163
 Millar T. J., Herbst E., 1990, *A&A*, 231, 466
 Muñoz Caro G.M., 2002, PhD thesis, Leiden Univ.
 Noll K.S. et al., 1995, *Science*, 267, 5202, 1307
 Okabe H., 1978, *Photochemistry of small molecules* (New York: John Wiley & Sons)
 Cecchi-Pestellini C., & Aiello S. 1992, *MNRAS* 258, 125
 Rivière-Marichalar P. et al., 2020, *A&A*, 642, A32
 Rocha W.R.M. et al., 2024, *A&A*, 683, A124
 Ruffle D.P., Hartquist T.W., Caselli P., Williams D.A., 1999, *MNRAS*, 306, 3, 691
 Sicilia D., Ioppolo S., Vindigni T., Baratta G.A., Palumbo M.E., 2012, *A&A*, 543, A155
 Sipillä O., et al., *in prep.*
 Sivaraman B., 2016, *J. Chem. Sci.*, 128, 1, 159
 Shen C. J., Greenberg J. M., Schutte W. A., van Dishoeck E. F., 2004, *A&A*, 415, 203
 Shingledecker C.N., Lamberts, T., Laas J.C., Vasyunin A., Herbst E., Kästner J., Caselli P., 2020, *ApJ*, 888, 52
 Slanger T.G., Black G., 1971, *JChPh*, 54, 1889
 Taillard A., Martín-Doménech R., Carrascosa H., et al., 2024, *A&A*, *submitted*
 Vidal T.H.G., Loison J.-C., Jaziri A.Y., Ruaud M., Gratier P., Wakelam V., 2017, *MNRAS*, 469, 1, 435
 Wakelam V., Castets A., Ceccarelli C. et al., 2004, *A&A*, 413, 609
 Wakelam V., Loison J.-C., Mereau R., Ruaud M., 2017, *Molecular Astrophysics*, 6, 22
 Ward M.D., Hogg I.A., Price S.D., 2012, *MNRAS*, 425, 2, 1264
 Yarnall Y.Y., Hudson R.L., 2022, *ApJL*, 931, L4
 Zhu Y.F., Gordon R.J., 1990 *JChPh*, 92, 2897
 Zhu C., Turner A.M., Abplanalp M.J., Kaiser R.I., 2018, *ApJSS*, 234, 15

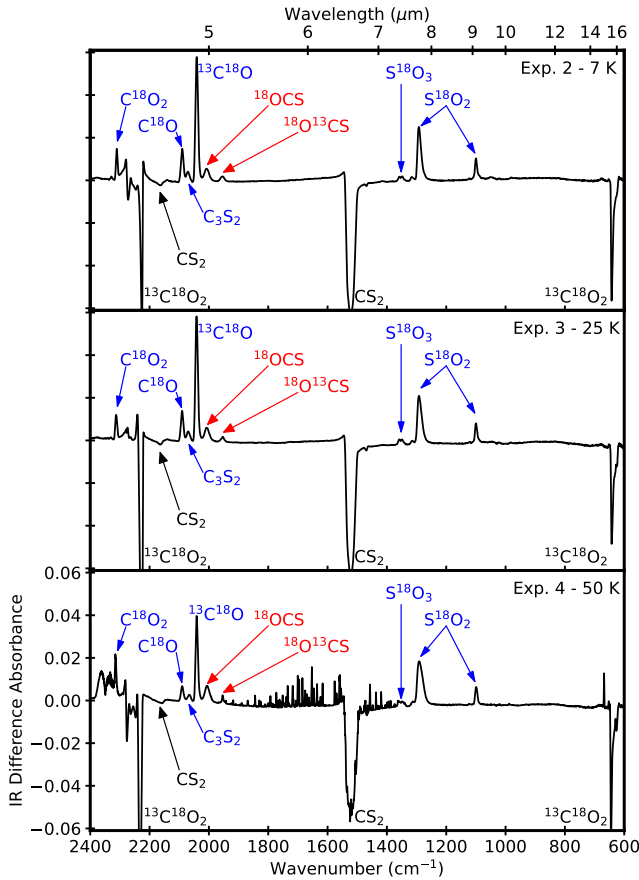


Figure A1. IR difference spectrum obtained upon 2 keV electron irradiation of a $^{13}\text{C}^{18}\text{O}_2:\text{CS}_2$ ice sample at 7 K (Exp. 2, top panel), 25 K (Exp. 3, middle panel), and 50 K (Exp. 4, bottom panel). Narrow features in the bottom panel are due atmospheric contamination in the IR detector chamber in this particular experiment. IR band assignments are indicated for the initial ice components (black), and ice chemistry products (blue), including the OCS isotopologs (red).

APPENDIX A: ADDITIONAL PLOTS OF THE 2 KEV ELECTRON IRRADIATION OF $^{13}\text{C}^{18}\text{O}_2:\text{CS}_2$ ICE SAMPLES AT 7–50 K

The IR difference spectra in the 2400–600 cm^{-1} range obtained upon 2 keV electron irradiation of $^{13}\text{C}^{18}\text{O}_2:\text{CS}_2$ ice samples at 7 K (Exp. 2), 25 K (Exp. 3), and 50 K (Exp. 4) are shown in Figure A1. The spectra did not present significant differences in this temperature range.

In addition to the thermal desorption of ^{18}OCS and $^{18}\text{O}^{13}\text{CS}$ shown in the main body of the manuscript (Fig. 2, bottom panels), desorption of the S-bearing products SO_2 and S_2 was also observed during warm-up of the irradiated ices. The corresponding TPD curves for the ice samples irradiated at 7 K (Exp. 1), 25 K (Exp. 3), and 50 K (Exp. 4) are shown in the top and bottom panels of Fig. A2. The small fraction of S^{18}O_3 molecules produced upon irradiation (Sect. 3.1) probably fragmented in the QMS and contributed to the S^{18}O_2 and S^{18}O signals. Thermal desorption of S^{18}O molecules from the ice could not be confirmed with the available data. Thermal desorption of C_3S_2 was not detected during warm-up of the irradiated $^{13}\text{C}^{18}\text{O}_2:\text{CS}_2$ ice samples, but it was observed in the $^{13}\text{C}^{18}\text{O}:\text{CS}_2$ experiments (Fig. C2, bottom panels).

APPENDIX B: DESORPTION OF MOLECULES DURING IRRADIATION OF $^{13}\text{C}^{18}\text{O}_2:\text{CS}_2$ ICE SAMPLES

As explained in Sect. 3.4, desorption of $^{13}\text{C}^{18}\text{O}$, C^{18}O molecules and $^{13}\text{C}^{18}\text{O}_2$ molecules was observed during irradiation of the $^{13}\text{C}^{18}\text{O}_2:\text{CS}_2$ ice samples (Fig. 9). This desorption was selective (no other species desorbed during irradiation), and took place only when the ice was being actively irradiated (the corresponding QMS signal decreased down to the background level during the irradiation pauses, as it occurs in VUV photodesorption experiments). The desorption of $^{13}\text{C}^{18}\text{O}$ and C^{18}O increased with the irradiation time in all experiments (probably due to the accumulation of molecules as they were being formed in the ice), and was more than an order of magnitude higher in the experiment at 50 K.

The QMS calibration process described in Martín-Doménech et al. (2024) should in principle be used only with integrated TPD curves, since the k_{CO} proportionality constant was derived from TPD calibration experiments. The desorption of molecules during irradiation of the $^{13}\text{C}^{18}\text{O}_2:\text{CS}_2$ ice samples might have followed different dynamics than the thermal desorption during warm-up of the ice samples, resulting in a different k_{CO} value. We note that, for example, k_{CO} derived from TPD experiments is different for different heating rates. In any case, we used the k_{CO} value presented in Sect. 2.5 to estimate the column density of $^{13}\text{C}^{18}\text{O}$ molecules desorbing during irradiation in Experiments 1–4 as a first approximation. To this purpose, we divided k_{CO} by the 2 K min^{-1} heating rate applied in the calibration experiments to obtain a new value of $5.75 \times 10^{-12} \text{ A min ML}^{-1}$, leading to the results presented in Sect. 3.4.

APPENDIX C: ADDITIONAL PLOTS OF THE 2 KEV ELECTRON IRRADIATION OF $^{13}\text{C}^{18}\text{O}:\text{CS}_2$ ICE SAMPLES AT 7–25 K

The IR difference spectra in the 2400–600 cm^{-1} range obtained upon 2 keV electron irradiation of $^{13}\text{C}^{18}\text{O}:\text{CS}_2$ ice samples at 7 K (Exp. 7), 15 K (Exp. 8), and 25 K (Exp. 9) are shown in Figure C1. The main differences between these spectra are shown in the top panels of Fig. 8, and discussed in the main body of the manuscript.

In addition to the thermal desorption of ^{18}OCS and $^{18}\text{O}^{13}\text{CS}$ shown in the bottom panels of Fig. 8, desorption of the S-bearing products SO_2 and C_3S_2 was also observed during warm-up of the irradiated ices. The corresponding TPD curves for the ice samples irradiated at 7 K (Exp. 7), 15 K (Exp. 8), and 25 K (Exp. 9) are shown in Fig. C2.

APPENDIX D: ADDITIONAL PLOTS OF THE 2 KEV ELECTRON IRRADIATION OF $\text{H}_2^{18}\text{O}:\text{CS}_2$ ICE SAMPLES AT 8–50 K

In addition to the thermal desorption of ^{18}OCS (Fig. 13), we also observed thermal desorption of S^{18}O_2 and S_2 during the TPD of the $\text{H}_2^{18}\text{O}:\text{CS}_2$ ice samples irradiated at 8 and 50 K. The corresponding TPD curves are presented in Fig. D1.

This paper has been typeset from a $\text{\TeX}/\text{\LaTeX}$ file prepared by the author.

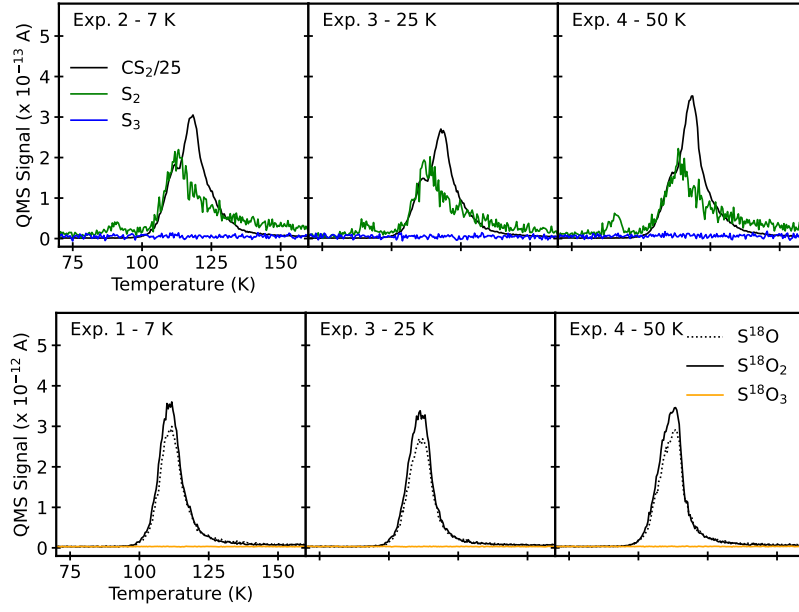


Figure A2. Top: TPD curves corresponding to CS_2 (black), S_2 (green) and S_3 (blue) molecules measured during thermal desorption of the $^{13}\text{C}^{18}\text{O}_2:\text{CS}_2$ ice samples irradiated at 7 K (Exp. 1, left panel), 25 K (Exp. 3, middle panel) and 50 K (Exp. 4, right panel). Bottom: TPD curves corresponding to S^{18}O_2 (solid black), S^{18}O_3 (orange), and the S^{18}O fragment (dotted black) during thermal desorption in Experiments 2 (irradiated at 7 K, left panel), 3 (25 K, middle panel), and 4 (50 K, right panel).

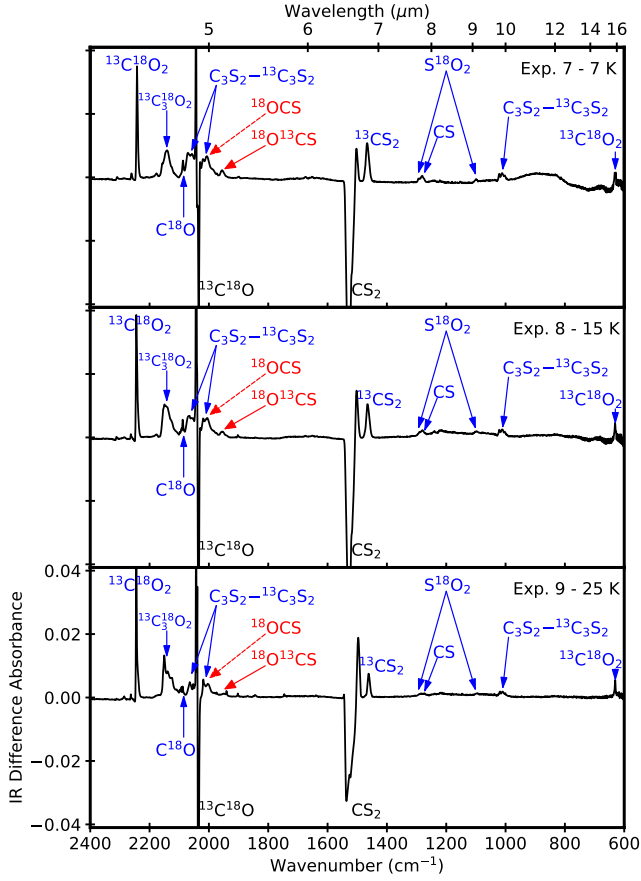


Figure C1. IR difference spectra obtained upon 2 keV electron irradiation of a $^{13}\text{C}^{18}\text{O}:\text{CS}_2$ ice sample at 15 K (Exp. 8, middle panel) and 25 K (Exp. 9, 25 K). The IR difference spectrum of the ice sample irradiated at 7 K (Exp. 7, top panel, also shown in Fig. 7) is presented for comparison. IR band assignments are indicated for the initial ice components (black), and ice chemistry products (blue), including the OCS isotopologs (red).

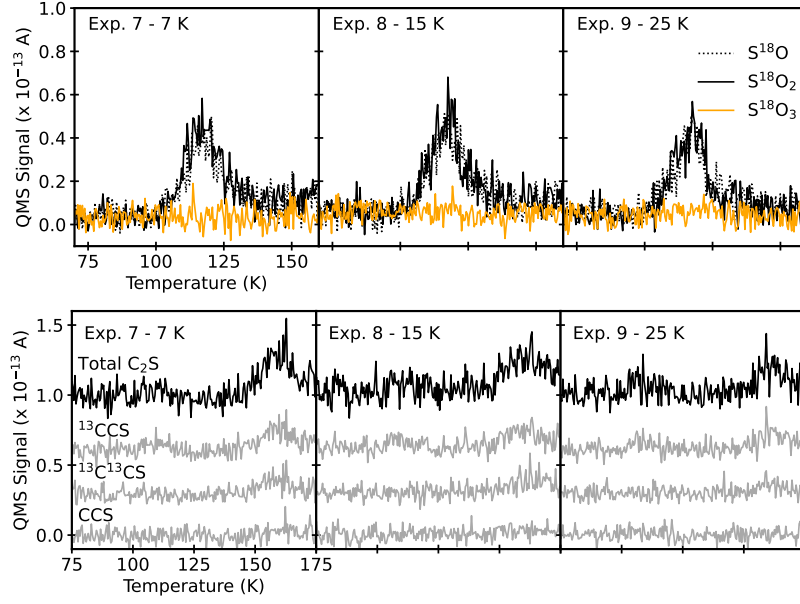


Figure C2. Top: TPD curves corresponding to S¹⁸O₂ (solid black), S¹⁸O₃ (orange), and the S¹⁸O fragment (dotted black) measured during thermal desorption of the ¹³C¹⁸O:CS₂ ice samples irradiated at 7 K (Exp. 7, left panel), 15 K (Exp. 8, middle panel) and 25 K (Exp. 9, right panel). Bottom: TPD curves corresponding to C₂S fragments of C₃S₂ isotopologs with different isotopic composition measured in the same experiments. The TPD curves are shifted for clarity. Note that for similar abundances of the different C₃S₂ isotopologs (Sect. 3.3), the C₂S fragment with one ¹³C was more abundant for statistical reasons.

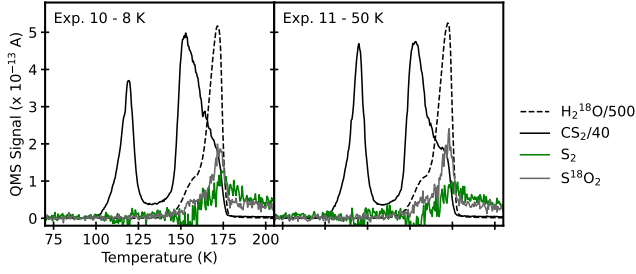


Figure D1. TPD curves corresponding to the remaining H₂¹⁸O (dashed black) and CS₂ (solid black), and the produced S¹⁸O₂ (gray) and S₂ (green), measured during thermal desorption of the H₂¹⁸O:CS₂ ice samples irradiated at 8 K (Exp. 10, left panel) and 50 K in (Exp. 11, right panel).